UNIVERSITY OF OKLAHOMA

GRADUATE COLLEGE

CALIBRATION AND CLUTTER CANCELLATION TECHNIQUES FOR ACCURATE WIDEBAND RADAR CROSS SECTION MEASUREMENTS

A THESIS

SUBMITTED TO THE GRADUATE FACULTY

in partial fulfillment of the requirements for the

Degree of

MASTER OF SCIENCE

By

RACHEL JARVIS

Norman, Oklahoma

2021

CALIBRATION AND CLUTTER CANCELLATION TECHNIQUES FOR ACCURATE WIDEBAND RADAR CROSS SECTION MEASUREMENTS

A THESIS APPROVED FOR THE
SCHOOL OF ELECTRICAL AND COMPUTER ENGINEERING

BY THE COMMITTEE CONSISTING OF

Dr. Jay McDaniel, Chair

Dr. Jessica Ruyle

Dr. Justin Metcalf

Acknowledgments

The support and encouragement from my primary advisor Dr. Jay McDaniel has been indispensable to my success as a graduate student and researcher. By trusting me to lead several aspects of this project, he gave me the opportunity to find my passion for research and realize the full extent of my capabilities. I would also like to thank Dr. Justin Metcalf and Dr. Jessica Ruyle for sharing their technical and professional expertise on this project as advisors. Our spirited scientific discussions are some of my favorite weekly activities.

The collaborative environment at the Advanced Radar Research Center (ARRC) provided access to my colleagues' invaluable collection of knowledge. In particular, Rylee Mattingly's positive demeanor and LabVIEW skills were very helpful during this project.

Finally, I would like to thank my parents, Marty and Karla Jarvis, and my grandparents, Jerald and Lois White, for their continued support throughout all of my academic endeavors.

This work was funded by the U.S. government under contract 2019-19012300001S.

Table of Contents

List of Tables

List of Figures

Abstract

The expected received power is a key design parameter when designing a radar system. The radar's receiver must be sensitive enough to detect the object of interest without being saturated by the highest received power. The object of interest's visibility to the radar is determined by its radar cross section (RCS), which is a function of the object's size, shape, material, and orientation as well as the polarization and frequency of the incident wave. Even for simple objects like spheres, calculating the RCS is cumbersome, and there are only closed-form solutions for a few geometries. Of the existing analytical solutions, almost all assume that the incident wavelength is much larger than the object. Simulations can be used to find RCS, but the computational requirements quickly increase with the object's size and complexity. The best method to determine the RCS of large, complex objects or any object over a wide bandwidth is measurement. There are many challenges that must be overcome to obtain accurate RCS measurements, especially when the RCS is measured over a wide bandwidth. Traditionally, these measurements are collected with two co-located antennas connected to a vector network analyzer. The signal received from the OUT is very small due to free-space path loss and cable loss, while the mutual coupling between the antennas and reflections from other clutter can be significant.

At the University of Oklahoma's Advanced Radar Research Center, a single measurement configuration is designed and tested to measure the RCS of a 6-inch sphere with less than 5% average error from 2-18 GHz. This accuracy is achieved

through strategic hardware selection, careful calibration, and clutter suppression algorithms in post-processing. Stepped Frequency Continuous Wave (SFCW) radar principles are applied to design the clutter suppression techniques, including vector background subtraction and time-gating. After verifying the validity of the measurement results with spheres, the techniques are applied to the measurement of distributed targets. Multiple spheres and an OU Skywalker unmanned aerial vehicle (UAV) are measured across angle with vertical and horizontal wave polarizations. The measurement frequency capabilities are then expanded by using single antenna reflection coefficient results to extract the RCS. This single-antenna configuration introduces new obstacles that are overcome to achieve an average error of less than 12.5% from 300-1000 MHz. With a few hardware alterations, the measurement bandwidth could be expanded even further to characterize the RCS values of interest more extensively.

Chapter 1

Introduction

Engineers use radar for various tracking, detection, and imaging applications across industries, including meteorology, defense, and remote sensing. To properly design a system for these purposes, the transmitter and receiver must be carefully designed for the specific use case. For example, the transmitted and received power levels of an automotive radar are different from an airborne radar. In each use case, the power received from objects far away is much smaller than the power received from scatterers close to the radar. The difference between the minimum and maximum signal is the dynamic range. The receiver must accommodate a substantial dynamic range by being sensitive enough to detect the object of interest without becoming saturated.

The radar range equation determines the expected power level that the receiver must detect. This equation contains known system parameters such as antenna gain and operating frequency and the range and radar cross section (RCS) of the object of interest. The RCS describes how much incident energy the object reflects back to the radar. If the RCS is larger than expected, the received power will be too high and saturate the receiver. On the other hand, the receiver will not be sensitive enough to detect the object if the RCS is smaller than expected.

The physical size of the object does not totally determine an object's RCS. The

energy backscattered from an object also depends on the shape, orientation, and material of the object, and the frequency and polarization of the incident wave; therefore, calculating an object's RCS becomes very complex. Electromagnetic simulators can overcome some of these challenges with modern computing capabilities but struggle with dielectric materials and electrically large geometries. Instead, the object's backscatter can be measured. The results of these measurements are often discussed in the open literature, but the details of the measurement process are not usually included [6] [7].

Obtaining highly accurate results over a large bandwidth further complicates the process. The signal's power must be greater than the thermal noise power to extract information from the desired signal. Losses that occur through free-space propagation and lossy coaxial cables diminish the desired signal's power, making it more challenging to maintain this ratio. These system losses increase with frequency, so the transmitted signal must be amplified to maintain the signal-to-noise ratio at high frequencies. On the other hand, mutual coupling between the two antennas and multi-path reflections are highest at the low frequencies, so the transmitted power is limited to avoid saturating the receiver. Moreover, these unwanted signals' power increases as a function of the transmit power, so amplifying the transmitted signal does not improve the desired signal's power relative to this clutter. Therefore, the challenge of balancing these power requirements to maintain the desired dynamic range becomes more difficult as the measurement frequency range is increased.

This thesis is concerned with overcoming the clutter challenges associated with reducing RCS measurement error. The measurements are conducted over as large of a frequency range as possible with vertically and horizontally polarized waves. The configuration needs to have the flexibility to measure a variety of objects of interest, including calibration spheres and the University of Oklahoma (OU) Sky-

walker unmanned aerial vehicle (UAV).

The following chapters describe the design and implementation of the measurement procedure. Chapter 2 presents the foundations of electromagnetic scattering. It describes an incident wave's interaction with an object and the mechanisms that scatter energy back towards the antennas. Then RCS calculation is introduced, and the RCS values of a sphere and a cylinder are derived.

Chapter 3 details the process of obtaining RCS values from the measured power. This process involves applying step frequency continuous wave radar principles to careful calibration techniques, including vector background subtraction and time-gating. This chapter concludes by presenting considerations for the physical measurement configuration.

Chapter 4 compares and contrasts two electromagnetic simulation softwares. Simulation performance is compared to analytically known values, and the practicality and limitations of simulating electrically large structures is examined.

In Chapter 5, the measurement methodologies discussed are applied to anechoic chamber measurements. Initially, a sphere is measured from 2-18 GHz across azimuthal angle to analyze the process's accuracy. Then, more complex objects are measured and compared to simulated values.

Chapter 6 explores expanding the measurement frequency capabilities below 2 GHz by using a single antenna reflection coefficient. This configuration has improved portability and affordability, but it also presents more thermal noise challenges.

Chapter 7 gives the thesis conclusion and proposes improvements and areas of future work.

Chapter 2

Background

In this chapter, electromagnetic scattering mechanisms are introduced and related to the resultant RCS of basic geometries. Because this work is concerned with RCS over a large bandwidth for various object sizes, the behavior of each scattering region described below is observed. Then the calculated RCS values are discussed for a few simple geometries of interest.

2.1 Electromagnetic Scattering

There are several different methods that an incident electromagnetic wave scatters off of an object. Backscatter is defined as the total amount of incident energy that is reflected back towards the antennas. The specific physics of the scattering depends on the electrical size, shape, and material. An object's electrical size is determined by the ratio of its physical size to the incident wavelength. For smooth objects, there are three primary scattering regimes: Rayleigh (low-frequency), Mie (resonance), and Optical (high-frequency).

2.1.1 Rayleigh Scattering

When the incident wavelength is much larger than any dimension of the object under test (OUT), the scattering falls within the Rayleigh regime. In this region, the phase of the incident wave over the extent of the object is almost constant, and the subsequent phase and amplitude of the induced current are also almost constant [5]. As a result, this problem is analyzed with static field principles. The shape of the OUT does not significantly affect these scattering phenomena, so it is possible to use scalar values instead of vector values. The quasi-static incident wave builds up opposing charges at the ends of the OUT, inducing a dipole moment p, which is defined by:

$$p = qd \tag{2.1}$$

where q is the charge of the particles and d is the separation between them [8]. The orientation of the incident wave plays a significant role in the dipole moment's magnitude because it determines which dimension the dipole moment is excited. Fig. 2.1 illustrates this concept. When the wave's polarization is perpendicular to the cylinder's length, as seen in Fig. 2.1a, there is only a small separation between the charges equal to the cylinder's diameter. Conversely, when the horizontally polarized wave is incident on the horizontal cylinder, as seen in Fig. 2.1b, the charge is separated across the cylinder's entire length. The scattered electric field (E_s) is proportional to the induced dipole moment, so more scattering is expected when the incident wave is polarized parallel to the OUT's maximum dimension.

In general, the reflected wave is a function of the current density. In this region, the charge (q) within the dipole moment reverses direction with the frequency of

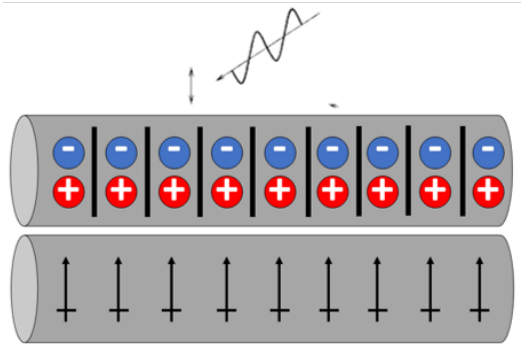

(a) Vertical Polarization

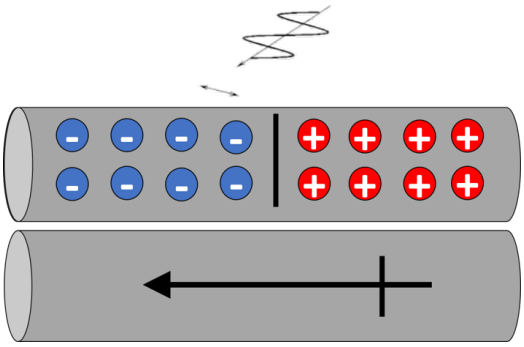

(b) Horizontal Polarization

Figure 2.1: The charge distribution and subsequent dipole moments excited on a carbon fiber rod for vertically and horizontally polarized incident waves

the incident wave, and the subsequent current density is

$$J = \frac{dq}{dt} = j\omega q \tag{2.2}$$

where ω is the angular frequency. The scattered electric field (E^s) is proportional to ωJ or $\omega^2 q$ [1]. Therefore, the scattered field increases proportionally to ω^2.

2.1.2 Mie Scattering and Optical Scattering

In the Mie (resonance) region, the OUT's size is between 1 and 10λ. Consequently the current's phase changes greatly across the object [1]. There are two primary scattering mechanisms in this region: surface waves and optical reflection.

The overall reflected wave is the result of the collective interaction of all of the waves. Surface waves travel along the outside of the conducting object and may interfere with other scattering mechanisms.

As the OUT's size exceeds 10λ, surface waves are still present, but optical scattering dominates the return. Therefore, this point is defined as the beginning of the optical region. There are many scattering phenomena in the optical region, including diffraction, end-region scattering, specular scattering, and multiple-bounce [9] [10]. Specular scattering and multiple-bounce are the most relevant to this work. A common example of specular scattering is light reflecting off a mirror. The incident wave obeys Snell's law, meaning that the reflected wave's angle is equal to the incident wave's angle [11]. Multiple-bounce results from specular scattering off of one object to another and then back towards the receiving antenna. The scattering is the most angle-dependent in this region because the current's phase progresses through several cycles due to the relatively small wavelength [5].

2.2 RCS Calculation

RCS is defined as "the ratio of the power scattered from an object in units of power per solid angle (steradian) normalized to the plane wave illumination in units of power per unit area" [12]. In other words, RCS is the ratio of the incident power density to the power density scattered by an object. In practice, RCS is used to determine an object's visibility to a radar. Mathematically, RCS (σ) is given by [13] to be:

$$\sigma = \lim_{R \to \infty} 4\pi R^2 \frac{|E_s|^2}{|E_i|^2} \tag{2.3}$$

where E_s and E_i are the incident and scattered electric field, respectively, and R is the distance between the object and the point of observation.

RCS is not just a function of an object's size but also depends on the object's material, shape, and orientation and the incident wave's frequency and polarization [5]. The electrical properties of the material, including permittivity, permeability, and conductivity, play an important role in scattering. Conductive metals such as aluminum efficiently reflect waves while dielectric materials with higher permittivity and loss absorb some of the incident wave and burn the energy as heat [1]. The smoothness of the material also determines the amount and direction of reflection. Surface roughness inhibits the coherency and flow of current on the object and also results in diffuse area or volumetric scattering, ultimately resulting in a smaller backscatter towards the radar [14].

The methods to solve for the scattered field from an object are the same as those used to solve the radiated field from an antenna. Similarly, analytical solutions are only available in a few cases, and some of these cases are discussed below. For most geometries, the differential and integral forms of Maxwell's equations are solved numerically [5]. Chapter 4 describes how electromagnetic solvers numerically solve these equations for arbitrary geometries.

2.3 Sphere Scattering

The sphere is a widely used object for scattering measurements because the symmetric geometry produces an angle-agnostic RCS and an almost constant RCS above a certain frequency. An infinite sum describes the radar cross section of a perfectly conducting sphere. The solution, called the Mie series, is given by:

$$\sigma = \frac{\lambda^2}{\pi}\left|\sum_{n=1}^{\infty}(-1)^n(n+\frac{1}{2})(b_n - a_n)\right|^2 \tag{2.4}$$

where

$$a_n = \frac{j_n(ka)}{h_n(ka)} \tag{2.5}$$

$$b_n = \frac{kaj_{n-1}(ka) - nj_n(ka)}{kah_{n-1}(ka) - nh_n(ka)} \tag{2.6}$$

and

$$h_n(x) = j_n(x) + iy_n(x) \tag{2.7}$$

where i is the imaginary number and ka is the sphere's electrical circumference, composed of the wavenumber k (where $k = 2\pi/\lambda$) and the sphere radius a [15]. Additionally, $j_n(x)$ and $y_n(x)$ are n-order Bessel functions of the first and second kinds, respectively, with argument x, and $h_n(x)$ is the spherical Bessel function of the third kind [16]. While an infinite sum is not practical to implement, a recursive approximation can be applied in MATLAB as described in [17].

Fig. 2.2 depicts the RCS of a sphere as a function of ka. In the resonance region,

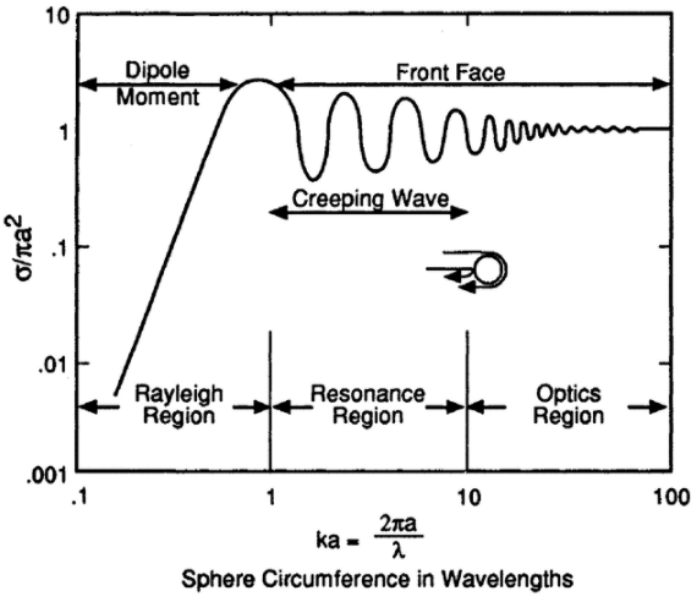

Figure 2.2: Radar cross section of a metallic sphere over the three scattering regimes [1]

the creeping wave travels to the back of the sphere and wraps around to the front. A creeping wave is a surface wave on the side of the object shaded from the antenna's illumination. The creeping wave phase depends on the frequency of the incident wave relative to the size of the sphere and constructively adds with the specular return when the creeping wave and specular reflection align in phase. Other times, the phase of one return lags the other, causing deconstructive interference. This alternating frequency-dependent interference causes the oscillatory RCS behavior. As the incident wave's frequency increases, the creeping wave's contribution is insignificant compared to the specular reflection. Once $ka = 1$, the sphere begins behaving with oscillatory RCS, signifying the Mie scattering region. Finally, the oscillations decay to an almost constant RCS value of πa^2, or the two-dimensional area of a circle, in the optical region at $ka = 10$. Now that computers can quickly calculate the varying RCS at lower frequencies, spheres can be used across all three scattering regimes making it an ideal object for RCS calibration purposes. However, minor changes in sphere size or frequency lead to significant RCS changes outside of the optical region, leaving potential for error.

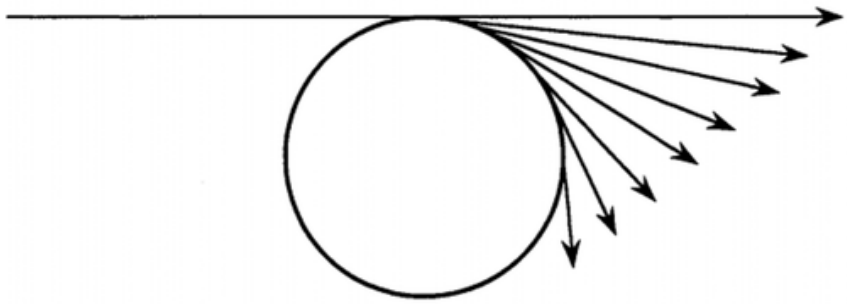

Figure 2.3: Creeping wave sheds energy as travel along the object [1]

2.4 Wire Scattering

The common closed-form solution for a cylinder's RCS assumes that the cylinder's diameter is at least 3.5 wavelengths [18]. When the diameter is instead small relative to a wavelength, the geometry resembles a wire. A generalized Van Vleck equation given in [2] approximates the RCS of a wire of length $(2l)$ and radius (a) to be:

$$\sigma = \frac{\lambda^2 cos^4\phi}{\pi K K^*} E E^* \tag{2.8}$$

where

$$K = 2log\left(\frac{2l}{a}\right) + 2log2 + \frac{a}{l} - \text{Cin}2(\beta - q)l - \frac{\sin(\beta+q)l - 1}{2(\beta+q)l} - \cdots$$
$$\frac{\sin 2(\beta-q)l}{2(\beta-q)l}\text{Si}2(\beta+q)l + \text{Si}2(\beta-q)l + \frac{\cos 2(\beta+q)l - 1}{2(\beta+q)l} + \frac{\cos 2(\beta-q)l - 1}{2(\beta-q)l} \tag{2.9}$$

$$\text{Cin}x = \int_0^x \frac{1 - \cos t}{t} dt \tag{2.10}$$

$$\text{Si}x = \int_0^x \frac{\sin t}{t} dt \tag{2.11}$$

$$E = \frac{\sin 2ql}{\cos\theta} - (T_1 + T_2)\frac{\sin(\beta+q)l}{1+\cos\theta} - (T_1 - T_2)\frac{\sin(\beta-q)l}{1-cos\theta} \tag{2.12}$$

and

$$\beta = \frac{2\pi}{\lambda} \tag{2.13}$$

$$q = \beta\cos\theta. \tag{2.14}$$

Fig. 2.4 compares the resultant RCS across incident angle in the "Generalized Van Vleck Results" to BRACT, which is a source distribution technique computer

program developed by MBAssociates in 1967. When the wave is incident upon

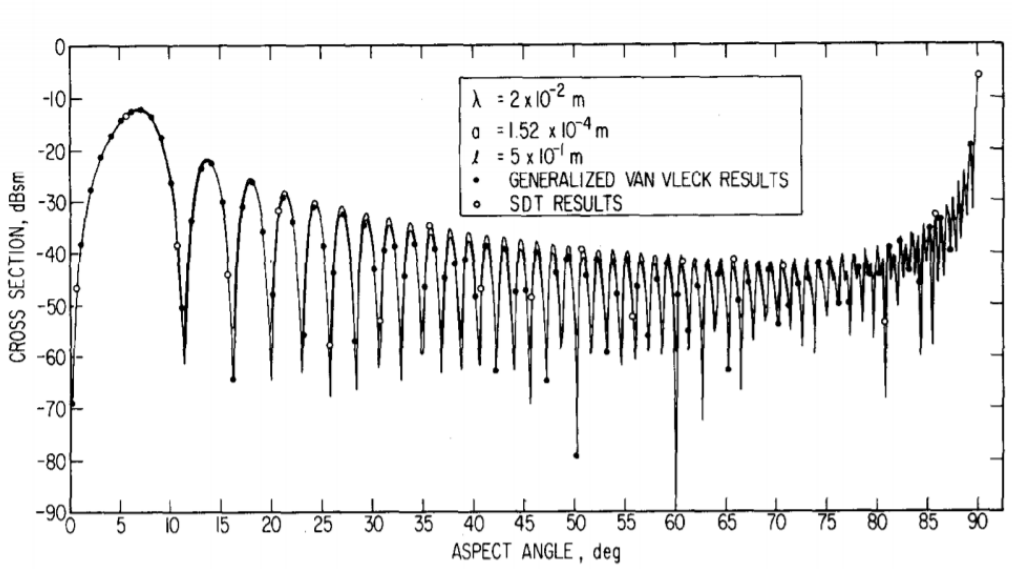

Figure 2.4: Monostatic cross section of a wire (linear polarization) [2]

the end of the wire, the RCS approaches negative infinity. The RCS reaches its maximum when the wave is normally incident and quickly decreases for angles off of broadside. The RCS drops by over 10 dBsm with only a few degrees of rotation.

2.5 Foam Scattering

Plastic foam is composed of many small beads with polymer cell walls and gas within the cells [18]. As a result, there are two methods of scattering: surface and volume reflections. Surface reflections are a coherent reflection of the wave from the outside of the foam, as shown in Fig. 2.5a. The reflection coefficient (Γ) describes the power reflected by foam with effective permittivity ε_f. At normal incidence, the reflection coefficient is given by:

$$\Gamma = \frac{1 - \sqrt{\varepsilon_f}}{1 + \sqrt{\varepsilon_f}} \tag{2.15}$$

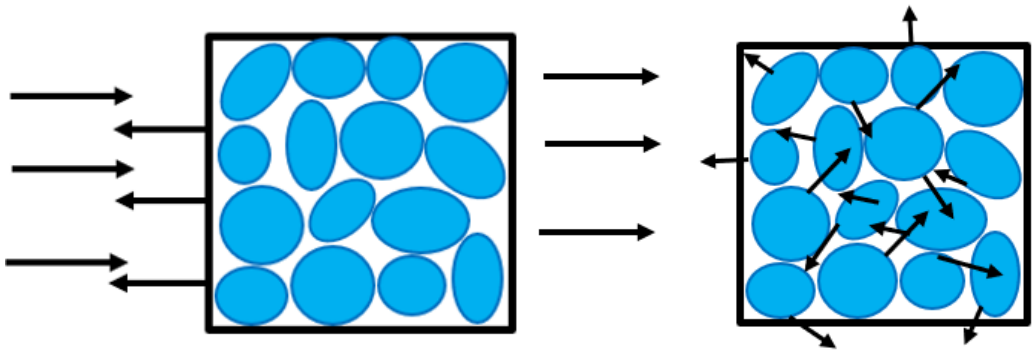

(a) Surface reflections (b) Volume reflections

Figure 2.5: Foam scattering mechanisms

meaning that the greater the effective permittivity relative to air, the more reflection that occurs. The permittivity of foam is generally very close to air, but the scattering is proportional to a combination of the surface area and the reflectivity. Even a structure with low reflectivity can have non-trivial scattering if there is a large surface area normal to the incident wave.

The other scattering mechanism is volume reflection, defined as the incoherent reflection from each of the numerous, randomly oriented beads within the foam, as shown in Fig. 2.5b. This scattering is difficult to calculate analytically, but it ultimately depends on the number of beads present to scatter the incident wave. The shape of the foam does not affect the amount of volume reflection. Instead, minimizing the overall volume of foam reduces the volume reflection. The trade-off of adding foam volume to create a strategic geometry for reducing surface reflections, and general material and shape considerations for an RCS measurement setup, is discussed in more detail in Section 3.3.

Chapter 3

RCS Extraction Methodology

This chapter describes how to convert complex power values to RCS. This process includes applying several radar concepts, careful calibration, and strategic measurement setup choices to accurately extract the RCS. Even in an anechoic chamber, where external noise sources are significantly reduced, internal clutter complicates the procedure and requires further analysis.

3.1 SFCW Principles

A vector network analyzer (VNA) operates in the same manner as a stepped frequency continuous wave (SFCW) radar. SFCW radar operates by sequentially transmitting and receiving N discrete frequencies, as illustrated across time and frequency in Fig. 3.1. The transmitted SFCW waveform, $s(t)$, is defined as

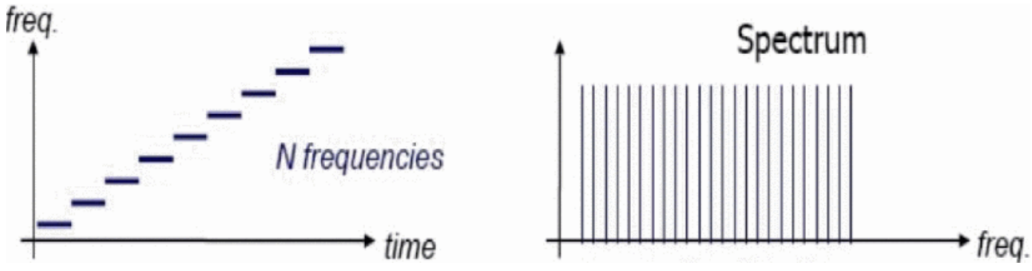

Figure 3.1: (a) Output step frequency, (b) Frequency spectrum of output [3]

$$s(t) = \frac{1}{\sqrt{T}} \sum_{n=0}^{N-1} \text{rect}\left(\frac{t - NT}{T}\right) e^{j2\pi(f_0 + n\Delta f)t} \tag{3.1}$$

where rect is the rectangular function, T is the pulse length, f_0 is the first pulse frequency, n is the pulse number, Δf is the frequency increment between pulses, and t is time. The received waveform, $s_r(t)$, is an amplitude-scaled copy of the transmitted waveform delayed by the round-trip propagation time, given by

$$s_r(t) = as(t - 2R/v_p) \tag{3.2}$$

where a is the received signal amplitude, R is the range from the port of the VNA to the scatterer, and v_p is the velocity of propagation. Because the range reference is at the port of the VNA instead of the transmit antenna, some of the wave's propagation is through the dielectric associated with the radio frequency (RF) coaxial cables. Therefore, within the cables, v_p is slower than the speed of free-space propagation. Careful attention must be given to this velocity of propagation difference during calculations.

The VNA demodulates the signal according to each step's carrier frequency. Each resulting sample of the baseband signal is expressed as

$$s(f_n) = e^{-j4\pi f_n R/v_p}. \tag{3.3}$$

Applying the Inverse Fast Fourier Transform (IFFT) to the received signal in (3.3),

the discrete-time signal $x(k)$ is given by:

$$\begin{aligned} x(k) &= \sum_{n=0}^{N-1} s(f_n) e^{j2\pi nk/N} \\ &= e^{-j\pi(N-1)(k_m-k)/N} e^{-j4\pi f_0 R/c} \frac{sin[\pi(k_m-k)]}{sin[\pi(k_m-k)/N]} \end{aligned} \tag{3.4}$$

where $k = 0, 1, ..., N-1$ and $k_m = 2RN\Delta f/v_p$. The first two terms describe the phase values, while the third term is the sinc-valued magnitude, which is the Fourier transform pair of a rectangular function in the frequency domain. The sinc function peaks when $k = k_m$. A more intuitive understanding of k_m will become clear after further analysis.

The phase (θ) of the baseband received signal in (3.3) is given by:

$$\theta = 4\pi f_n \frac{R}{v_p} \ . \tag{3.5}$$

For two consecutive frequencies (f_1 and f_2), the phase difference ($\Delta\theta$) becomes:

$$\Delta\theta = \theta_2 - \theta_1 = \frac{4\pi R}{v_p}(f_2 - f_1) = \frac{4\pi R}{v_p}\Delta f \tag{3.6}$$

Solving for R,

$$R = \frac{v_p \Delta\theta}{4\pi\Delta f} \ . \tag{3.7}$$

Due to the periodic nature of sinusoids, the baseband signal's phase values repeat each time θ progresses 2π. Therefore, the possible unambiguous range values are defined for values of $0 < \theta \leq 2\pi$ with the maximum unambiguous range (R_{max}) given by:

$$R_{max} = \frac{v_p}{2\Delta f} \ . \tag{3.8}$$

If the OUT lies beyond R_{max}, the return folds into a closer range bin, causing distortions in time-domain processing. R_{max} encompasses the propagation from the port of the VNA to the OUT, so accounting for the slower propagation through the coaxial cables is especially important in (3.8).

The range resolution (ΔR) describes the radar's ability to separate the return from two scatterers. The Rayleigh criterion defines the resolution as the distance between the waveform's peak and its first null [19]. The resolution is related to the bandwidth (B) by:

$$\Delta R = \frac{v_p}{2B} = \frac{v_p}{2N\Delta f} \ . \tag{3.9}$$

Using this relation, k_m in (3.4) can be re-written as $\frac{R}{\Delta R}$. In other words, $x(k)$ peaks at the index corresponding to the scatterer's range. Therefore, the matched filter for the VNA measurements and SFCW radar in general is simply the IFFT.

The final applied radar principle is the signal-to-noise ratio (SNR), which is the desired signal power divided by the noise power. If the desired signal power falls below the noise floor, no amount of post-processing can extract the information. The receiver noise power (P_n) is given by:

$$P_n = kFTB \tag{3.10}$$

where k is Boltzmann's constant, F is the noise figure of the measurement unit (VNA or radar), T is the noise temperature in Kelvin, and B is the receiver's bandwidth, not the transmit waveform's frequency span. Increasing the transmit power and adding amplifiers can help overcome thermal noise, as long as the amplifiers are applied before the desired signal falls below the thermal noise floor. Another strategy is coherent integration which averages several measurements together over

time. However, this technique only improves the SNR if the noise is uncorrelated between the measurements. Multi-path reflections occur when the transmitted wave arrives travels more than one path to arrive at the receive antenna. In addition to traveling directly to the OUT and back to the antennas, the wave may bounce off of the chamber walls, floor, and ceiling. While the foam absorbers attenuate the signal, they do not absorb all of the incident power. Increasing the transmit power also increases the power of the reflections, so a higher transmit power does not improve the SNR. Furthermore, coherent integration does not provide any improvements in the desired signal strength because the multi-path reflections are correlated between measurements. Therefore, the clutter must be suppressed using other post-processing techniques discussed next.

3.2 Calibration

Proper calibration is essential for obtaining accurate RCS measurements. The measurements used in this procedure are the magnitude and phase of S_{21} collected with a VNA. S_{21} is the ratio of power received at port 2 to the power transmitted at port 1. The received power is much smaller than the transmitted power at the VNA ports because of losses throughout the system. As the wave propagates through the air, it spreads spherically. Consequently, only a fraction of the transmitted wave arrives at the OUT, and only a fraction of the backscattered wave arrives at the receive antenna. This spherical spreading loss is referred to as free-space path loss, and it is a function of the operating wavelength and distance of the wave's propagation. The signal is also attenuated as it travels through coaxial cables, and the attenuation is highly frequency-dependent. For example, the total cable loss increases by 65 dB from 2-18 GHz in the setup described in Section 5.1. Other scatterers like

the chamber walls and the support structures, as well as mutual coupling between the co-located antennas, can interfere with the small quantity of received power. Therefore, techniques in post-processing are necessary to isolate the desired return from all of these additional undesired signal sources.

The calibration procedure used in this work is outlined in Fig. 3.2 and discussed in more detail below. The tasks are arranged into three main steps: background subtraction, time-gating, and calibration set creation. Each of these will be further discussed.

3.2.1 Vector Background Subtraction

The most simple clutter cancellation technique to implement is vector background subtraction. First, S_{21} is collected from the empty chamber, including the OUT support structure. Next, the calibration object is placed inside the chamber and measured, followed by the OUT. After the measurement's collection, the mag-

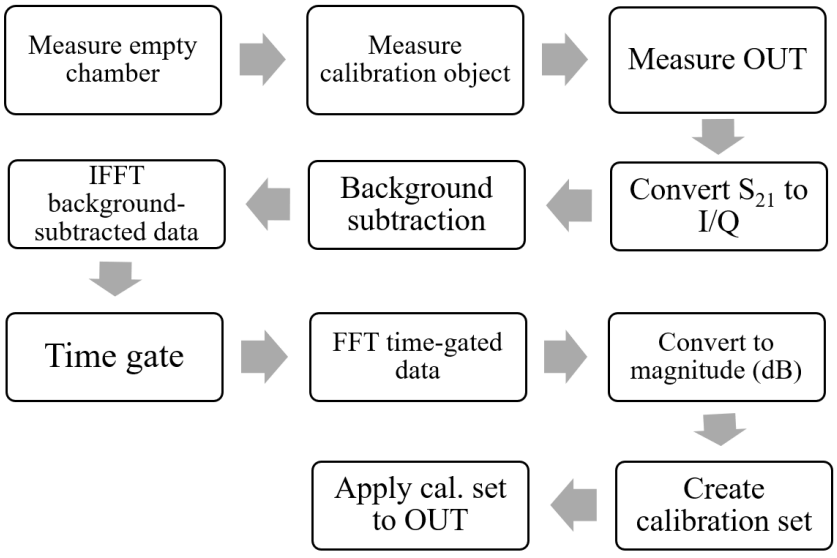

Figure 3.2: Steps for RCS calibration with background subtraction and time-gating [4]

nitude and phase of the S_{21} values are converted to in-phase and quadrature (I/Q) components with the relation S = I + jQ where j is the imaginary number. Then, the S_{21} magnitude (S) and phase (θ) are converted to in-phase and quadrature (I/Q) using the following:

$$I + jQ = S\cos(\theta) \; + \; jS\sin(\theta) \; . \tag{3.11}$$

The empty chamber's I/Q data is subtracted from the calibration object and OUT I/Q data. This creates the "background subtracted" datasets that will be referred to throughout this work. If using multiple support structures, each must be measured and used as the background measurement for each respective OUT. This process eliminates a significant amount of clutter, but it is not perfect because of shadowing and multi-path effects [20].

3.2.2 Time Gating

The measurements in this work are collected in a continuous wave manner, meaning that the VNA is always transmitting and receiving signals. One consequence of this configuration is signal leakage from the transmit antenna to the receive antenna. Even if the VNA were operating in a pulsed mode, to eliminate the mutual coupling between the antennas, the pulse would have to be a fraction of a microsecond because of the small measurement range swath. Instead, the signal is filtered in time to only include returns from the desired ranges of interest in post-processing using a technique called time gating. Temporal filtering suppresses clutter not already removed by background subtraction and is necessary to accurately extract the desired signal.

As discussed in 3.1, the VNA receives a copy of the transmitted waveform from

each scatterer with a phase shift dependent on each scatterer's range. The sum of each received frequency step measurement populates the frequency domain over the measured bandwidth. This can be viewed as a sampled rect function defined as:

$$\begin{aligned} rect(f) &= s(f), \quad f_1 \leq f \leq f_2 \\ rect(f) &= 0, \quad elsewhere \end{aligned} \tag{3.12}$$

where s(f) is the complex-valued power and f_1 and f_2 are the beginning and ending frequencies of the measurement bandwidth. The Fourier transform pair of the rect function is a sinc function [21]. Therefore, applying the IFFT to the background-subtracted, frequency-domain measurements produces a sinc function for each received copy of the transmitted waveform. Each sinc function's peak occurs at the index that corresponds to the time delay of the received waveform according to (3.4). Because the velocity of propagation is known, peaks in the temporal domain provide the range to each scatterer. As the Fourier uncertainty principle states, a wider measurement bandwidth creates a wider rect function, which creates a narrower sinc function and consequently a finer resolution in the temporal domain. This intuitive interpretation agrees well with the inverse relationship between bandwidth and range resolution described in (3.9).

The OUT's temporal location (τ) can be determined analytically by calculating the delay of propagation through the cable lengths between the antennas and VNA as well as the range between the antennas and the OUT as follows:

$$\tau = \frac{2R}{v_p} \, . \tag{3.13}$$

This calculation can be laborious because the exact relative permittivity and length of the cables may be unknown. Instead, comparing measurements of various-sized

objects, each placed one at a time on the OUT pedestal, can indicate when the OUT return arrives. If the entire setup remains the same except for the OUT, the magnitudes of everything in the time domain should remain the same except for the peak corresponding to the time of the OUT's return. This method is not perfect because shadowing and multi-path may alter the test environment, but these variations are typically minor compared to the changes in the return of interest.

The simplest temporal filter is defined by a simple rect function defined by:

$$\begin{aligned} w(n) &= 1, \quad r_1 \leq n \leq r_2 \\ w(n) &= 0, \quad elsewhere \end{aligned} \tag{3.14}$$

where r_1 and r_2 are the beginning and ending indices in the time domain. The filter's value is 1 over the ranges of the desired signals, and the undesired return ranges are removed by being convolved with a value of 0. This temporal filter is commonly referred to as a window. The shape of the window to apply for time gating depends on the temporal resolution, relative temporal locations of nearby undesired reflections, and relative sizes of the OUTs. When the temporal resolution is coarse such that the OUT lies within a single range cell, the time-domain measurement is multiplied by the simple rect function described in (3.14). As the resolution is improved, more sophisticated windows are implemented. A tapered window, such as a Hanning window, mitigates the distortions at the edges of the frequency spectrum inherent to Fourier analysis [22]. The coefficients of the Hanning window are defined by:

$$w(n) = 0.5\bigg(1 - \cos\big(2\pi\frac{n}{N}\big)\bigg), \quad 0 \leq n \leq N \tag{3.15}$$

where the length of the window is $N + 1$ [21]. With extremely fine temporal resolution, reflections from different-sized objects do not arrive in the same range bin.

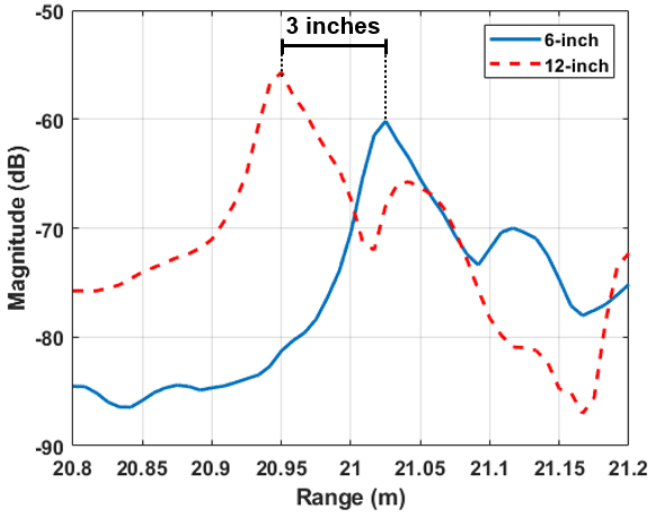

Figure 3.3: The return of two spheres of different diameters in the time domain after background subtraction measured from 2-18 GHz

Fig. 3.3 illustrates this situation. The return from a 6-inch sphere arrives after the 12 inch sphere's return. This delay corresponds to the difference in the spheres' radii. Applying a tapered window attenuates the returns unevenly. Alternatively, a hybrid window is created by convolving a Hanning window with a rectangular window. The taper on the sides still reduces edge effects while the flat center supports disparate target sizes.

3.2.3 Calibration Set Creation

Modeling the power throughout the system provides insight into the relationship between the power transmitted, power received, and RCS. To begin, the transmitted power density at range R from an isotropic antenna transmitting a total power of P_t Watts is calculated by distributing the total power across the surface area of a sphere with radius R. Mathematically, [23] defines this as

$$\text{Isotropic transmitted power density} = \frac{P_t}{4\pi R^2} \quad \text{W/m}^2. \tag{3.16}$$

For practical measurements, the power is focused towards the OUT using a directive antenna with gain G. Assuming the antenna's direction of maximum radiation intensity is pointing at the OUT, the peak transmitted power density (Q_t) is the power incident upon the OUT and is given by:

$$Q_t = \frac{P_t G}{4\pi R^2} \quad \text{W/m}^2. \tag{3.17}$$

For simplicity, it is assumed that the transmitted wave is incident upon a single discrete point scatterer. As defined in Section 2.2, the RCS describes how much energy the OUT can collect and reradiate isotropically. The isotropically reradiated power (P_b) is

$$P_b = \frac{P_t G \sigma}{4\pi R^2} \quad \text{W}. \tag{3.18}$$

To find the backscattered power density (Q_b), defined as how much of the power is reradiated towards the receive antenna, P_b is divided by the surface area of a sphere to get:

$$Q_b = \frac{P_t G \sigma}{(4\pi)^2 R^4} \quad \text{W/m}^2. \tag{3.19}$$

The effective aperture (A_e) describes an antenna's capacity to collect power. Using this quantity, the power captured by the receive antenna (P_r) is

$$P_r = \frac{P_t G A_e}{(4\pi)^2 R^4} \quad \text{W}. \tag{3.20}$$

The antenna's effective aperture is related to its gain and the operating wavelength (λ) by [13]

$$A_e = \frac{\lambda^2 G}{4\pi} \quad \text{m}^2. \tag{3.21}$$

Inserting this relation into (3.20), the received power is

$$P_r = \frac{P_t G^2 \lambda^2 \sigma}{(4\pi)^2 R^4} \quad \text{W}. \tag{3.22}$$

Dividing both sides by P_t and including system losses (L), σ is related to the ratio of $\frac{P_r}{P_t}$ by the radar range equation

$$\frac{P_r}{P_t} = \frac{G^2 \lambda^2 \sigma}{(4\pi)^3 R^4 L} = k\sigma \quad \text{W}. \tag{3.23}$$

All of the variables except for the power ratio and σ remain constant regardless of the OUT, and they can be combined into a single, frequency-dependent constant k.

The time-gated S_{21} measurements are inserted for P_r/P_t, and k is the calibration set. The calibration set is created by subtracting the actual RCS values (in dB) from the magnitude of the time-gated calibration object measurement. This actual RCS can be based on calculated or simulated values. Alternatively, a measured dataset can be used as the actual RCS if the calibration object has been professionally

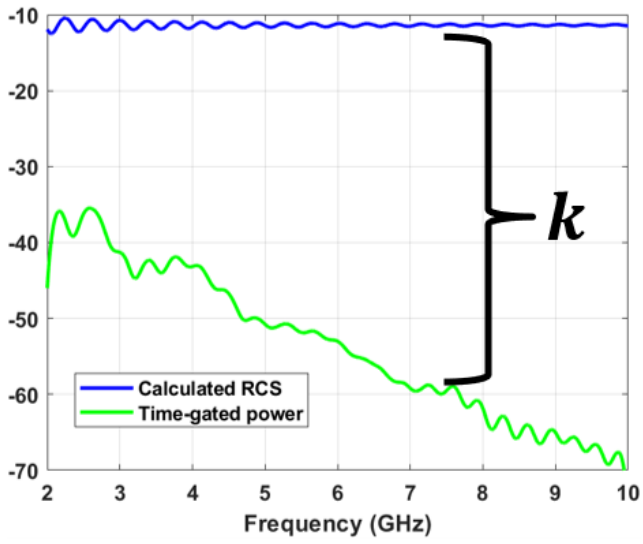

Figure 3.4: Time-gated power measurement and calculated RCS of a 12-inch sphere

measured in a calibrated setting. Therefore, it is best to choose a calibration object with an analytically known RCS, such as a sphere or cylinder, which are commonly used for RCS calibration. Finally, (3.23) is solved for the OUT's unknown σ by subtracting the calibration set from the time-gated OUT measurement.

3.3 Measurement Setup

Properly selecting the test hardware and arrangement is equally as important as the processing. The antennas must be spaced in a quasi-monostatic configuration to extract the monostatic RCS. However, closer proximity between the antennas results in more coupling between them. Moreover, the antenna beamwidth must be wide enough such that the entire OUT lies within the antenna's 3dB beamwidth, but not too wide as to limit additional multi-path clutter reflections. The linear width (L) of the beam when it is incident on the OUT is found from the half-power angular beamwidth (θ) using the relation

$$L = R \tan(\theta/2) \tag{3.24}$$

where R is the range from the antennas to the OUT. For both the transmit and receive antenna to fully illuminate the OUT, the condition

$$L \geq \frac{D+S}{2} \tag{3.25}$$

must be satisfied, where D is the OUT's width, and S is the spacing between the antennas.

The distance between the antennas and OUT also has an impact on the measurement accuracy. RCS is a far-field quantity, so it is assumed that the wave incident

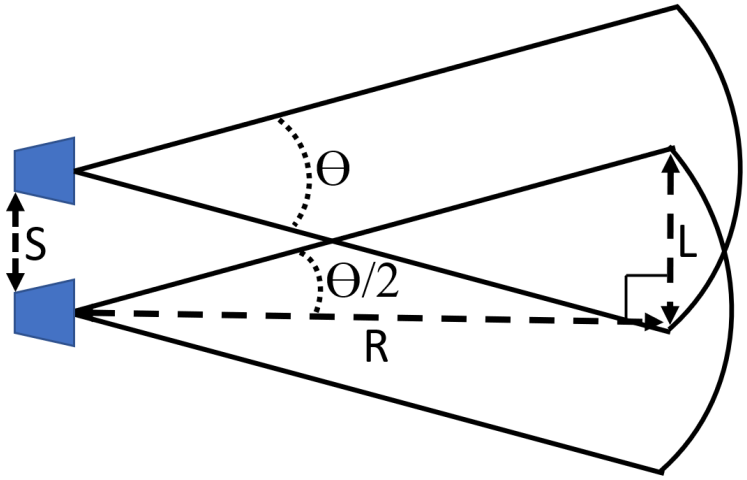

Figure 3.5: Geometry of antenna beamwidth intersection

upon the OUT is planar. The wave propagating from the antennas forms contours of equal phase defined by a sphere centered at the antenna. As the wave radially expands, the spherical wave eventually appears as a plane wave when a small segment is observed. For the OUT to be considered in the far-field, the spherical wave must travel a sufficient distance to appear approximately planar when incident upon the OUT. The phase of a plane wave is equal along a flat plane perpendicular to the wave's direction of propagation. Because the incident wave is not perfectly planar, the phase, and subsequently, the electric field is not the same along the length of the OUT. Therefore, the wave's interaction with the OUT is different at a finite range than the infinite range of the RCS definition in (2.3). Fig. 3.6 depicts the phase error (Δ), which is the difference in phase of the incident wave at the OUT's center compared to the phase at the ends of the OUT. There are differing standards for tolerable phase error. Classically, the measurement range must be greater than the far-field range (R_{FF}) given by:

$$R_{FF} = \frac{2D^2}{\lambda} \tag{3.26}$$

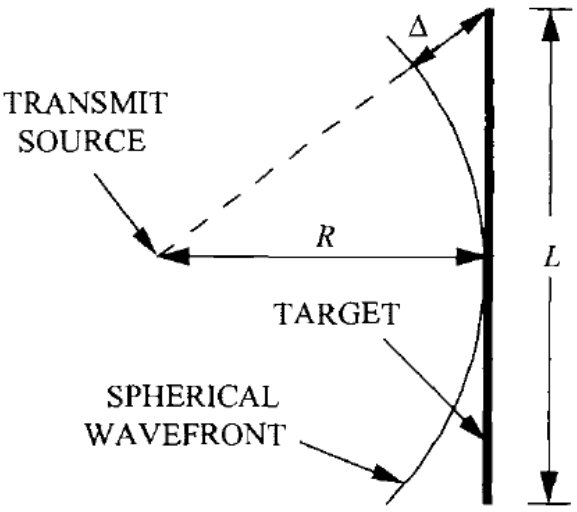

Figure 3.6: Phase error limitation for a far-field measurement [5]

where D is the maximum dimension of the OUT and λ is the wavelength corresponding to the highest operating frequency [6]. This specification gives a one-way phase error of $\frac{\pi}{8}$ radians. If an OUT is 0.5 m wide, R_{FF} is 3.3 m at 2 GHz and 30 m at 18 GHz. Other experts aim for a round-trip phase error below $\frac{\pi}{8}$ radians which coincides with

$$R_{FF} = \frac{16D^2}{\lambda} \tag{3.27}$$

as a minimum far-field range [5]. In practice, obtaining accurate measurements is still possible when the range to the antenna is even smaller than the less-stringent former criterion, especially for curved spherical surfaces [1]. However, it should be noted that minimizing the distance to the OUT drastically improves the power received because it reduces the R^4 term in the denominator of (3.23). Thus, it is often desirable to minimize the distance between the antennas and the OUT to have sufficient SNR in post-processing as long as the phase error is tolerable.

Once the antennas are arranged to be the appropriate distance from each other and the OUT, the final setup element that must be considered to minimize mea-

surement error is the structure that holds the OUT. An ideal support structure is as electrically transparent as possible. This principle includes selecting a material with a permittivity that is as close to air as possible. The material must also be able to provide enough support for the weight of each OUT. Depending on the application, foam columns, string supports, or metal pylons hold the OUT in place [18]. In this work, a foam pedestal sufficiently supports the size and weight of the OUTs. As discussed in Section 2.5, the total backscatter from the foam is a function of both surface and volume reflections. If the foam's effective permittivity is 1.1, then (2.15) states that 2.4% of the incident wave is reflected. Volume reflections cannot be avoided; they can only be minimized by reducing the volume of material in the structure's construction. Therefore, the pedestal's design focuses on reducing surface reflections.

While (2.15) describes the fraction of the incident wave reflected from a given material, the pedestal's size determines how much of the incident wave is interacting with the boundary. Therefore, two structures constructed with the same material reflect the same fraction of the incident wave, but the larger structure intercepts more energy and subsequently reflects more energy. The shape of the pedestal determines where the incident wave travels after interacting with the structure. The reflected wave's propagation direction is determined by the transmitted wave's angle of incidence and the shape of the foam. If the foam is a smooth surface normal to the incoming wave, all 2.4% of the wave is reflected back towards the antennas. By tapering the column, there are still volume reflections from each foam bead, but the oblique incidence directs the coherent surface reflection away from the antennas. Ultimately, prioritizing a reduction in surface reflections by adding tapering to the structure is more beneficial than minimizing the amount of material because surface reflections are summed coherently while volume reflections add together

incoherently. In other words, a tapered cylinder reflects less back to the antenna than a narrower cylinder with no tapering [18].

The tradeoff between construction practicality and optimal shaping is considered when designing each dimension of the foam support structure. Ideally, the pedestal's height holds the OUT as far as possible from any other scatterers including chamber walls and rotary machines. In practice, creating a very tall pedestal can be expensive and can increase the time required to swap out the OUT on top of the pedestal. The top of the pedestal must be wide enough to hold the OUT securely, and the size of the pedestal's base is designed to provide the desired tapering angle.

Selecting the width of the pedestal's base requires consideration of the operating frequency because the size of the base determines how steep the tapering is along the foam column. At low frequencies, the far-field criterion states that the incident wave is approximately planar across the full support structure. In the operating frequencies of this design, the foam structure's length is much larger than the incident wavelength, so optical approximations are implemented to understand the surface reflections. These approximations separate the incident wave into discrete beams that reflect specularly off of the foam. Therefore, the tapering angle simply determines the angle of the reflected plane wave's propagation, as shown in Fig. 3.7. The reflection near the top of the pedestal travels above the co-located transmit and receive antennas. Reflections originating from the lower portion of the pedestal may arrive back at the antennas. However, these returns are separated temporally from the OUT's return because the change in height creates a larger radial distance.

At higher frequencies, the incident wave may not appear to be planar across the full height of the pedestal. Using (3.26), an 18 GHz wave incident upon a 1 m object cannot be approximated as planar until it has propagated 120 m. This means that the incident wave front is still approximately spherical when it arrives at the

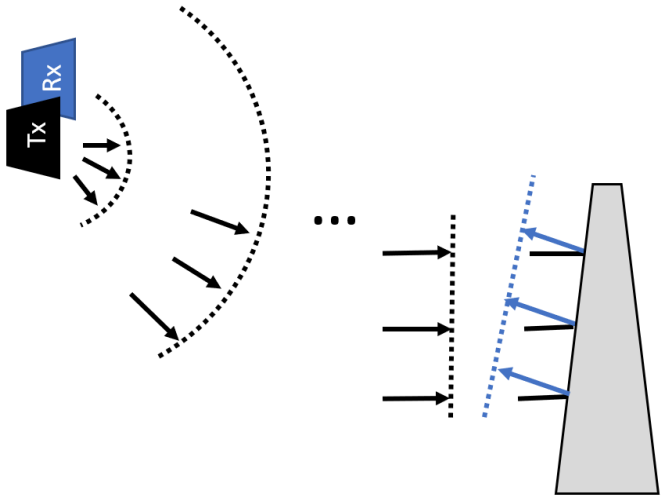

Figure 3.7: Incident and reflected plane wave when foam pedestal is well into the far-field region and the dotted lines represent contours of constant phase

foam support, as shown in Fig. 3.8. The same dimensions as the plane wave case are used, and the direction of the reflected wave is shown in Fig. 3.8a. At some angles near the top of the pedestal, the signal is reflected directly back towards the

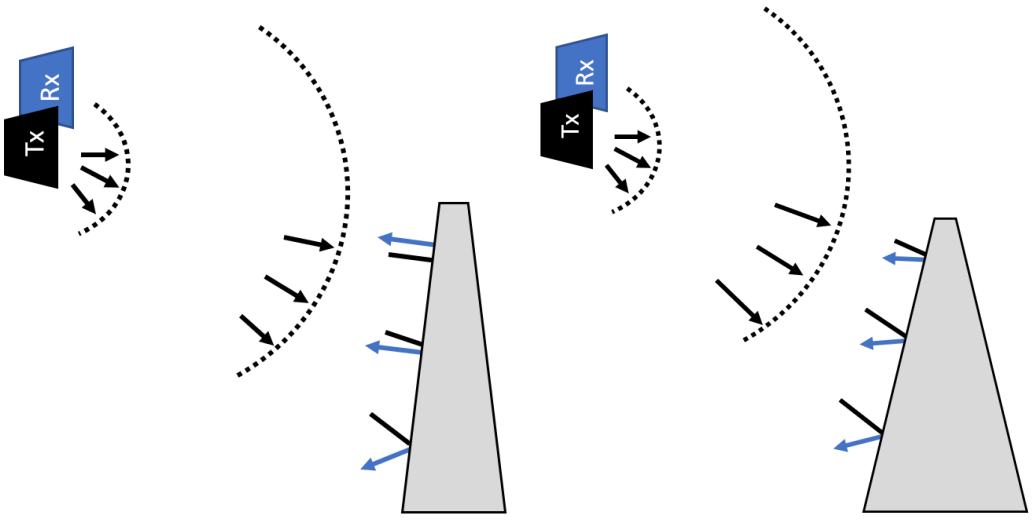

(a) Original Base

(b) Wider Base

Figure 3.8: Incident and reflected wave when the foam pedestal does not meet the far-field criterion with two different pedestal base widths where the dotted lines represent contours of constant phase

antennas. Because the OUT sits on top of the pedestal, the surface reflection and the OUT return appear very close in time and are difficult to separate during time-gating. By increasing the width of the pedestal's base, the incident wave is directed downward at all points along the height of the column, as shown in Fig. 3.8b. Thus, it is beneficial to add some incoherent foam volume reflections near the base of the pedestal to prevent surface waves from reflecting directly toward the antennas.

Chapter 4

RCS Simulation

In this chapter, the methods to simulate RCS are discussed and compared. As seen in Section 2.2, calculating RCS can be very computationally intensive, even for simple geometries. As computing power becomes more widely available, electromagnetic simulation is gaining popularity to estimate the RCS of electrically large, complex geometry, and distributed objects. Choosing a solver is a trade-off between simulation time, RAM usage, and accuracy. The results of different solvers are compared to each other and to analytical values. In this work, a 512 GB RAM computer with an 18-core processor and dual-16 GB GPUs is used to for simulations. To further validate the simulations, the next chapter compares the simulated results to measurements.

4.1 FEKO

Altair FEKO simulates the electromagnetic scattering by numerically solving the integral formulation of Maxwell's equations using the method of moments (MoM). This method solves for the surface current, making it ideal for metal objects where the current only exists on the outer surface [24]. As a result, a radiation boundary does not need to be defined. First, the scattered electric field (E^s) and

magnetic field (H^s) are calculated using the electric and magnetic field integral equations. Assuming a perfectly conducting surface, the integral equations may be simplified because there is no tangential electric field. The specialized equations are given by:

$$\mathbf{E^s} = \int_S [-j\omega\mu\mathbf{J}\Psi \; + \; \frac{1}{\varepsilon}\rho\nabla\Psi] \; dS \tag{4.1}$$

$$\mathbf{H^s} = \int_S \mathbf{J} \times \nabla\Psi dS \tag{4.2}$$

where μ is the permeability, $\mathbf{J}$ is the current density, Ψ is the spherical Green's function, ε is the permittivity, and ρ is the charge density [1]. Boundary conditions are applied, and then the surface currents and scattered fields are calculated. The far-field Green's function gradient is applied because only the far-field values are desired. Finally, (2.3) is used to relate the scattered electric field to RCS.

There are various strategies for simulating large models in FEKO, summarized in Table 4.1. The multilevel fast multipole method (MLFMM) reduces the computational demand by calculating the interaction between groups of basis functions instead of between individual basis functions [25]. This method uses the same size of mesh as the standard solver. The higher-order basis function (HOBF) solver further reduces the computational reduction, if necessary. HOBFs increase the mesh's segment size on electrically large objects to reduce the number of unknowns [26].

Electrical Size (λ)	**Solver Type**	**Mesh Size**
< 3	Standard	Standard
$3 - 6$	MLFMM	Standard
$3 - 8$	HOBF	Fine
$8 - 17$	HOBF	Standard
> 17	Ray Tracing	Fine or Standard

Table 4.1: The FEKO solver types and mesh sizes used for various object electrical sizes

Finally, ray tracing applies the reflection and refraction behavior from optics. This method assumes that the object is electrically large enough to approximate the incident wave as having a negligible wavelength.

4.2 HFSS

ANSYS High-Frequency Structure Simulator (HFSS) solves the differential form of Maxwell's equations and boundary conditions using the finite element method (FEM). This method separates the region into subregions called finite elements. After solving the equations at the nodes connecting the subregions, the method interpolates the current distribution's values within each subregion at each node [27]. This collection of elements and nodes is called a mesh. Each element's contribution adds together to form a global matrix of equations that describes the entire region. Boundary conditions are applied, and the equations are iteratively solved [28]. Then, the solver repeats this process for a finer mesh. If the difference in results is below the user-determined convergence threshold, then the simulation is complete. If not, then the mesh is refined to obtain more accurate values.

Instead of solving for the surface current like FEKO, HFSS solves Maxwell's equations in a 3-dimensional volume. Therefore, a radiation boundary or perfectly matched layer (PML) is needed to define the region to solve for the fields. To ensure that the region captures all relevant phenomena, this boundary should be at least $\lambda/4$ away from the OUT at all incident frequencies [29]. When simulating over a large bandwidth, the incident wavelength can change by an order of magnitude or more. Constructing a boundary that exceeds the $\lambda/4$ spacing increases the amount of mesh for HFSS to solve, adding unnecessary computational complexity. For this reason, simulation time and memory requirements are minimized by partitioning the band-

width into smaller frequency ranges, each with an appropriately-sized region.

Electrically large structures inherently occupy a greater volume, requiring more mesh. Consequently, minimizing the region's spacing does not sufficiently reduce the computational requirements. Less-stringent convergence standards lower the number of passes and consequently the size of the adaptive mesh. A coarser mesh sacrifices some accuracy, but simulating certain objects may be impossible without this tradeoff. If further efficiency is needed, a physical optics solver is available for electrically large structures. The current on the portions of the geometry illuminated by the incident wave is proportional to the magnetic field intensity, and the shadowed regions are assumed to have no current [5]. As a result, this estimate does not accurately represent the surface currents. This method is not as accurate, and it only works well for perfect electric conductor (PEC) structures [29].

4.3 Application

In addition to changing the solver settings in FEKO and HFSS, simplifying the model further reduces the computational requirements. This simplification can include approximating a conductive metal as PEC, adding lines of symmetry, or only including the largest scattering contributors in the model. For example, the 3D-scanned model of the OU Skywalker UAV, shown in Fig. 4.1, is so complex that even loading the structure into the simulator is difficult. Instead, the model only includes the hypothesized primary scatterers. The majority of the UAV's frame is foam, which is almost electrically transparent. The placement of electronic components such as cameras, GPS, etc., varies across different builds. The propeller placed in the back is typically plastic, and its curved geometry is not expected to scatter much energy back to the antennas. Therefore, the only consistent compo-

Figure 4.1: 3D-scan of the OU Skywalker UAV

nents expected to reflect a significant amount of incident energy are the carbon fiber rods running through the center of the UAV and the metal motor, as seen in Fig.4.2.

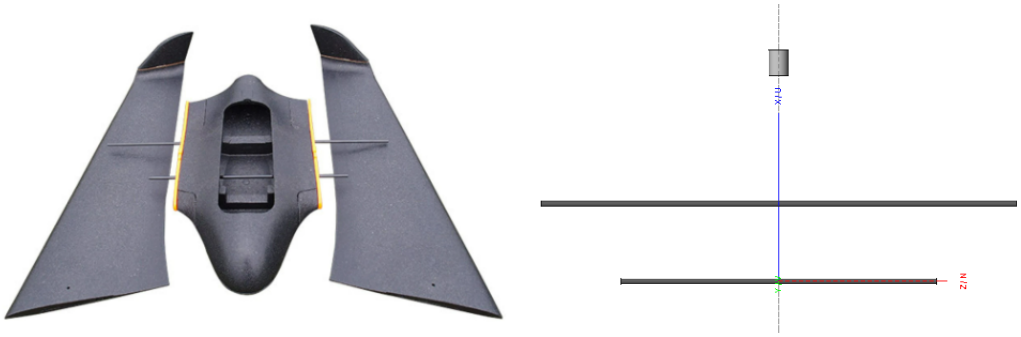

(a) Actual (b) FEKO Model

Figure 4.2: (a) the UAV foam frame with carbon fiber rods running through the center and (b) the FEKO model of two parallel carbon fiber rods with an aluminum cylinder representing the motor

Initially, to validate the solver methods' accuracy, a metal sphere's RCS is simulated because its RCS is analytically known. The traditional HFSS solver did not converge for the sphere simulation. Instead, the HFSS Integral Equation (IE) solver, which utilizes MoM, is implemented. It can be seen in Fig. 4.3 that the

simulated RCS from both solvers aligns almost perfectly with the analytical values. The HFSS IE solver eventually becomes too computationally intensive to complete

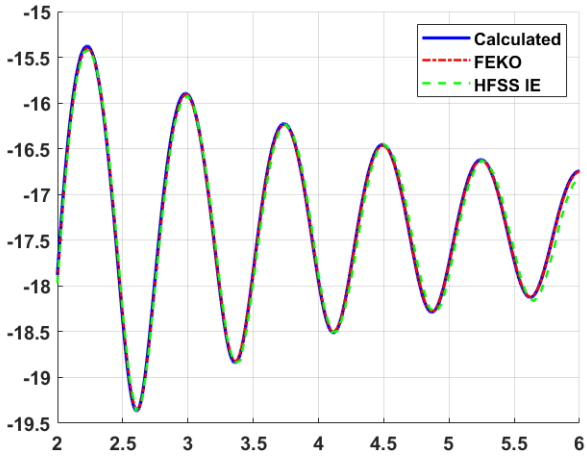

Figure 4.3: Simulated RCS of a 6-inch sphere compared to calculated

simulations at higher frequencies. FEKO simulations of a 6-inch sphere are completed from 2-18 GHz, as shown in Fig. 4.4. The results align almost perfectly with the calculated values at the lower frequencies, but they begin to deviate slightly

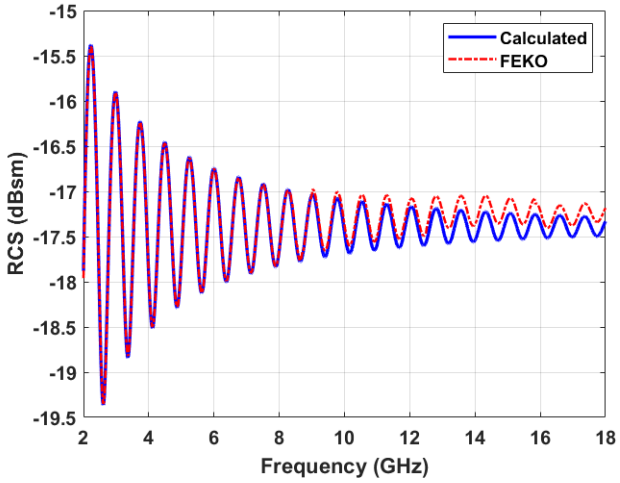

Figure 4.4: Simulated RCS of a 6-inch sphere compared to analytically calculated RCS

around 9 GHz. Using a coarser mesh to make the simulations computationally feasible introduced this offset at the higher frequencies. Overall, the shape of the results is correct, and the offset from calculated values is only a fraction of a dBsm. Now that a computational analysis has been completed for a simple PEC sphere across a wide bandwidth, the knowledge gained is used to simulate the UAV. This verification is important since simulating the UAV model is more difficult because the carbon fiber rods are a dielectric material instead of a conducting metal, and the rods are electrically large. Ultimately, FEKO is the only solver able to simulate the UAV model without exceeding the available computational resources. Section 5.6.2 presents the simulation results and compares them to measurements. The simplified model's validity is more easily evaluated with a side-by-side comparison of the simulated and measured results.

Chapter 5

Measurements

This chapter applies the RCS extraction methodology described in Chapter 3 to measurements taken in an anechoic chamber at the University of Oklahoma. The measurement of a 6-inch diameter sphere calibrated with a 12-inch diameter sphere provides a quantitative assessment of the measurement accuracy because the sphere's RCS is analytically known.

5.1 Test Setup Evolution

While the fundamentals of the measurement setup remained the same throughout this work, several components were modified over time to achieve better results. In each setup iteration, two antennas are mounted in quasi-monostatic configuration on one end of the far-field chamber and connected through a bulkhead to a calibrated Agilent N5222A PNA. The OUT is placed on an azimuthal rotation pedestal 6.8 m away from the antennas. The signal is attenuated greatly by spherical spreading loss in the two-way path across the chamber and by the long length of cable traveling between the antennas and through the bulkhead to the VNA ports outside the chamber. There is a 20 dB Keysight 83006A amplifier built into the chamber before the transmit antenna to compensate for this. Additionally, an amplifier is placed after

the receive antenna to prevent the returned signal from falling below the thermal noise floor before it reaches the VNA, as seen on the platform in the lower right of Fig. 5.1.

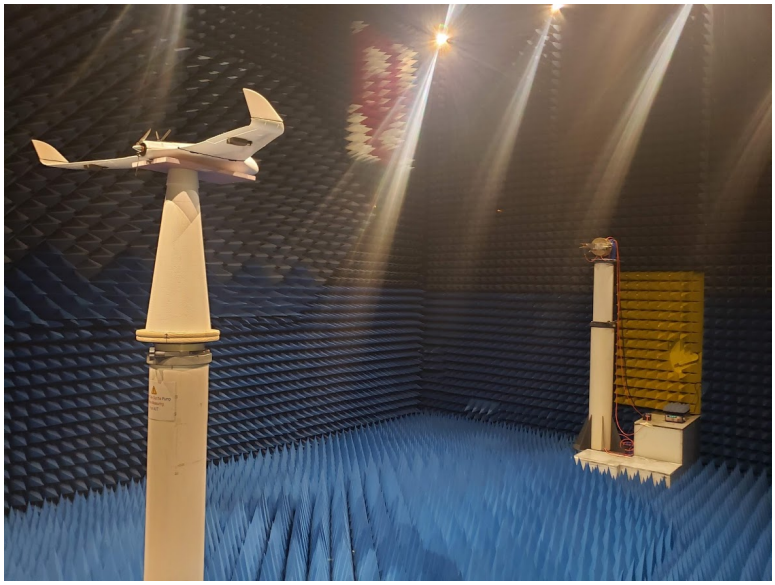

Figure 5.1: Final configuration of chamber measurement setup

Originally, the OUT was mounted on a pedestal composed of foam blocks, as shown on the left of Fig. 5.2. Even though this is a low-density foam pedestal, the flat edges produce a broadside reflection back to the antennas. Because of the pedestal's proximity to the OUT, these reflections shadow the desired return. A custom truncated cone pedestal purchased from WeCutFoam is constructed from 1.5 pounds per cubic foot expanded polystyrene (EPS) foam, as shown on the right in Fig. 5.2 to reduce broadside reflections. Spheres are placed directly into the indent on top of the pedestal, and other objects are mounted with a 3-D printed cover designed to create a flat surface. Objects are securely attached to the cover with velcro or glue, and covers are swapped out quickly for expeditious transitions between OUTs.

Ultimately, the measurement system implements two ultra-wideband Microwave

Figure 5.2: Old (left) and new (right) target support structures [4]

Vision Group dual ridge horn SH2000 antennas. Wideband horns have lower gain than narrower band antennas, but they allow a single test setup to be used from 2-18 GHz and have a large enough beamwidth to capture large OUTs fully. Initially, the receive amplifier was a 20 dB Custom MMIC CMD192C5 amplifier. To further improve the noise figure and to compensate for the low antenna gain, the receive amplifier is replaced with a more powerful 38 dB Mini-Circuits ZVA-183G-S+ amplifier. The anechoic chamber absorbing foam is supplied by Microwave Vision Group [30].

5.2 Single Sphere Measurement

The 38 dB amplifier, ultra-wideband antennas, and custom foam support structure are used to measure a 6-inch sphere calibrated with a 12-inch sphere in the large anechoic chamber at the Advanced Radar Research Center (ARRC) with various levels of post-processing. The measured RCS is very inaccurate after only ap-

plying the calibration set, as seen in Fig. 5.3. Without background subtraction and

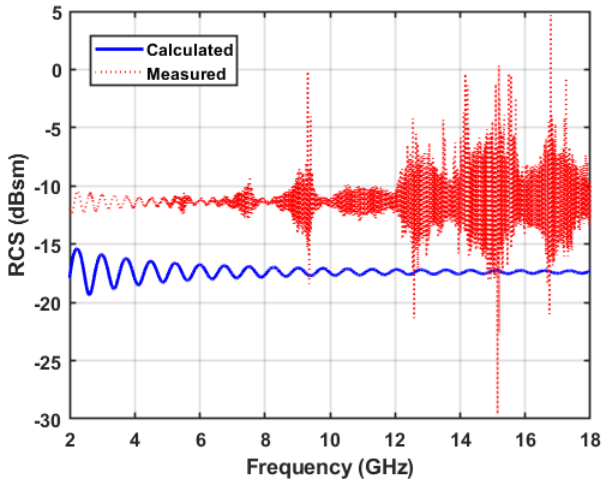

Figure 5.3: The measured RCS of a 6-inch sphere calibrated with a 12-inch sphere using no background subtraction or time-gating compared to analytically calculated results [4]

time-gating, the resultant RCS closely resembles the RCS of the 12-inch calibration sphere at low frequencies because the antenna coupling dominates the received signal. Fig. 5.4 illustrates this behavior, where the "Raw" trace is the output of the IFFT of the raw S_{21} values. The peak at 220 ns is from the antenna coupling, and the peak at 242 ns is a reflection from the platform holding the amplifier below the antennas. The peak from the mutual coupling is 15 dB higher than the desired return from the OUT at 263 ns. As a result, the received signal remains almost the same regardless of which OUT is inside the chamber, so swapping out the 12-inch sphere for the 6-inch sphere does not substantially impact the signal's overall magnitude. In this situation, the calibration set reflects the difference between the calculated sphere RCS and the antenna coupling power rather than the difference between the calculated sphere RCS and the returned power from the sphere. As a consequence of this error, the final extracted RCS is essentially be identical to whatever item is used as the calibration object.

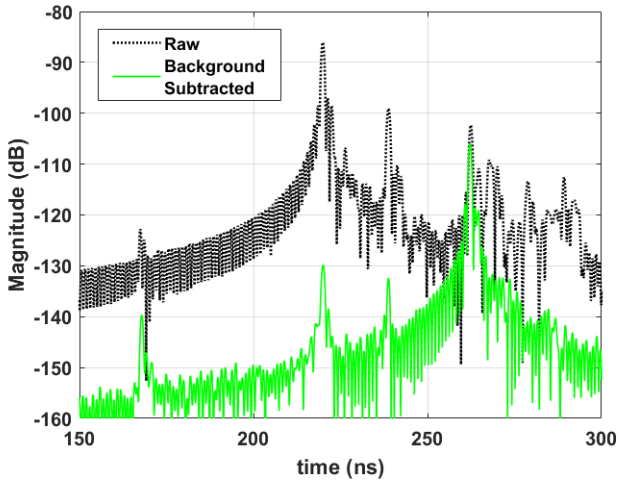

Figure 5.4: The matched filter output from a 6-inch sphere measured from 2-13 GHz with and without vector background subtraction [4]

The error between the calculated and measured RCS is a function of the difference between the calibration object and OUT's RCS values. Therefore, the difference between calculated and measured RCS is not an effective indicator of the accuracy of measurements processed by only applying a calibration set. After applying background subtraction, the desired return is the primary contributor to the overall return, as seen in the "Background Subtracted" trace in Fig. 5.4. Now, the total return varies as a function of the item in the chamber, and the calibration set that follows can correctly extract the RCS of the OUT. The background-subtracted measurements will serve as the baseline for comparison to other measurement configurations.

While vector background subtraction significantly increases the SNR around the OUT, there is still some residual clutter. The resultant RCS after calibration and background subtraction is still noisy, but it is now centered around the correct values, as shown in Fig. 5.5. The significant error below 6 GHz is from residual antenna coupling due to the larger antenna beamwidth at lower frequencies. The

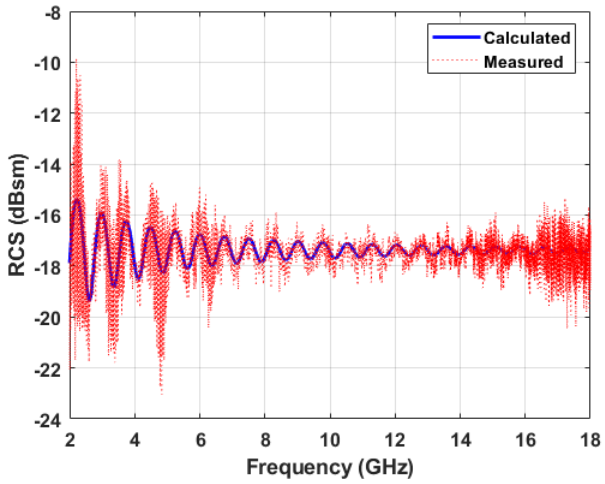

Figure 5.5: The measured RCS of a 6-inch sphere calibrated with a 12-inch sphere after vector background subtraction with no time-gating compared to analytically calculated results [4]

cable loss and free-space path loss increase with frequency, so the SNR of the measurement is degraded as frequency increases. As a result, the error increases above 14 GHz as the thermal noise begins to dominate the measured signal. Overall, the average error is 3.2 dBsm from 2-18 GHz.

After both time-gating and vector background subtraction are implemented to isolate the return from the OUT, the measured RCS aligns well with the theoretical values, as seen in Fig. 5.6. The measured RCS error increases slightly with frequency as the system losses increase, but the overall average error is only 0.21 dBsm. The former setup yields a tolerable error level for some measurement applications, but making a few changes produces highly accurate measurements.

While optimal post-processing techniques play a large role in measurement accuracy, the physical test environment also has a significant effect. Fig. 5.7 shows measurements collected with two different test setups. The “Original” trace was taken using a 20 dB amplifier on receive and the foam block support structure, and the “Improved” trace was taken with the 38 dB receive amplifier and custom trun-

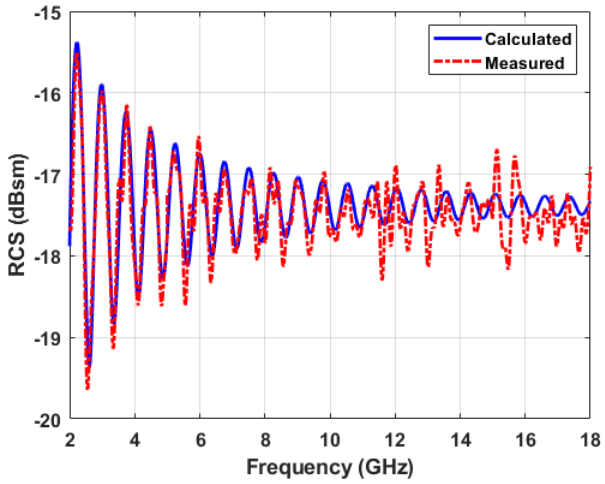

Figure 5.6: The measured RCS of a 6-inch sphere calibrated with a 12-inch sphere after background subtraction and time-gating compared to analytically calculated results [4]

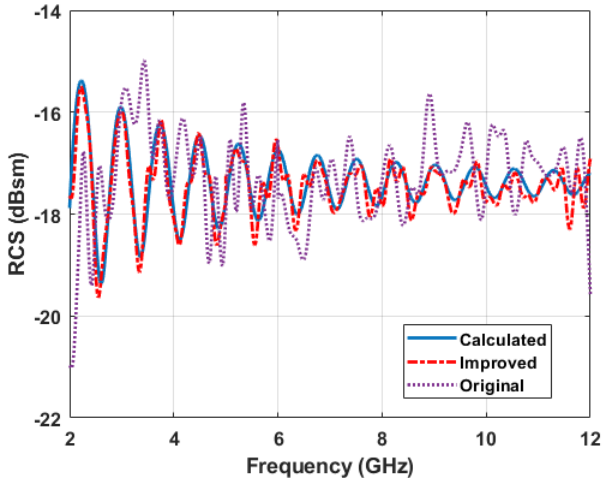

Figure 5.7: The measured RCS of a 6-inch sphere calibrated with a 12-inch sphere using two different support structures and amplifiers on receive compared to analytically calculated results [4]

cated cone support structure. The original setup yields an average error of 9.4% or 0.8 dBsm from 2-12 GHz, which is an acceptable value for some applications. By upgrading the hardware, the improved setup measurement error is only 2.4% or 0.21 dBsm using the same post-processing techniques.

Even with optimal processing, achieving these high-accuracy results is not possible if the calibration measurements are not taken correctly. The humidity and temperature of the chamber change over time. Therefore, background subtraction measurements must be collected each day for proper clutter suppression. Fig. 5.8 compares the measured RCS of a sphere processed with an empty chamber measurement taken the same day to when the empty chamber measurement is taken two days after the OUT measurement. The average error with a same-day empty chamber measurement is 0.389 dBsm, and the error increases to 0.965 dBsm with the delayed empty measurement.

5.3 Clutter Suppression Strategies

It is not always possible to take measurements in an ideal anechoic chamber setup. In particular, antenna coupling and large scatterers near the OUT make taking accurate measurements more difficult. If sufficient resolution is available, most

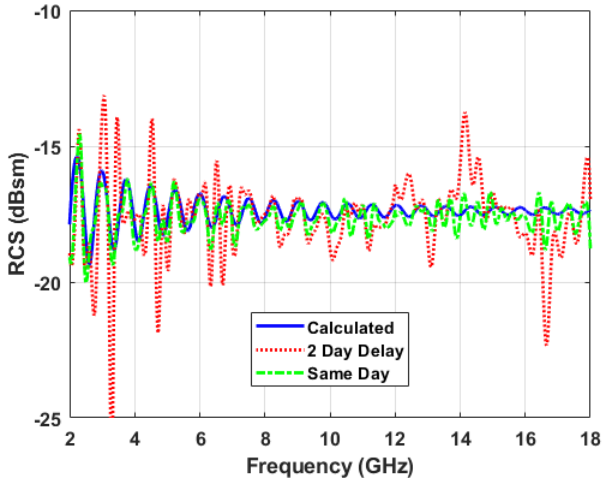

Figure 5.8: The measured RCS of a 6-inch sphere calibrated with a 12-inch sphere using an empty chamber measurement taken the same day as the OUT measurement compared to an empty chamber measurement taken 2 days apart from the OUT measurement and analytically calculated results

clutter can be suppressed in post-processing. If not, physical isolation strategies are necessary.

5.3.1 Antenna Isolation Strategies

The half-power beamwidth of the ultra-wideband antennas used for the far-field chamber measurement setup exceeds 130° from 2-4 GHz. The antennas must be placed near each other to maintain a quasi-monostatic configuration for measuring monostatic RCS. Because of the close proximity and wide beamwidth, there is a great deal of mutual coupling, or leakage, between the transmit antenna and the receive antenna. There are two strategies for reducing the effects of the antenna coupling: physical barrier and post-processing time-gating.

If there is enough temporal resolution to separate the antenna coupling from the OUT's return, the leakage can be removed in post-processing with time-gating. If time-gating is not possible, placing a baffle, which is a conductive barrier, between the antennas prevents some leakage. If the baffle is too large, the substantially distorted beam pattern corrupts the transmitted and received signal. Due to its finite size, the baffle cannot perfectly isolate the antennas from each other. The simulated electric field's magnitude between two ultra-wideband horn antennas viewed from above is shown in Fig. 5.9.

It is evident that the baffle between the antennas blocks most of the transmitted waves, but there is still some leakage around the edge of the baffle. A baffle is constructed to be lightweight and feasible for the current test setup with thin cardboard covered with aluminum foil and copper tape and placed between the two antennas, as seen in Fig. 5.10a. Another option to reduce leakage is to place metal panels on the antennas' sides, as shown in Fig. 5.10b. The simulated baffle reduces the

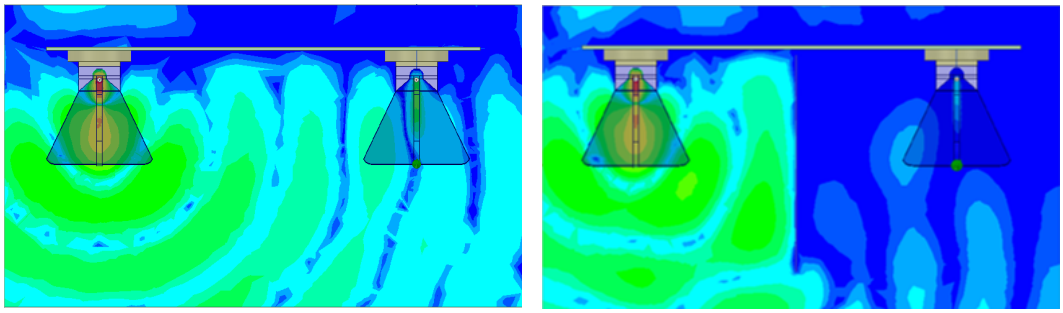

(a) Without Baffle (b) With Baffle

Figure 5.9: HFSS simulation of the electric field of two SH-2000 horn antennas at 2.5 GHz with and without a 15 cm by 15 cm aluminum baffle

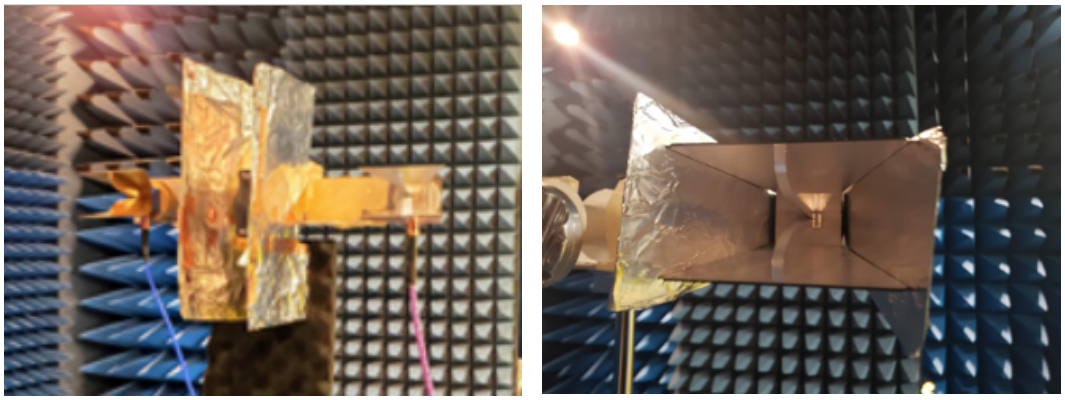

(a) Baffle (b) Side Panels

Figure 5.10: Setup of two SH-2000 horn antennas with two isolation schemes: an aluminum baffle in (a) and aluminum panels on the sides of the antennas in (b)

mutual coupling power between the two antennas by an average of 15 dB, as seen in Fig. 5.11. Implementing the baffle from Fig. 5.10a in measurement reduces the antenna coupling by 6 dB while increasing the proportion of the overall energy received from the sphere, as shown in Fig. 5.12. Additionally, the creeping wave received right after the specular sphere return is visible immediately after the sphere's primary peak about 12 dB below the main return's magnitude. While the sphere is the dominant peak in the range profile after adding the baffle, the antenna coupling is still a substantial contributor. Therefore time-gating is still necessary to produce

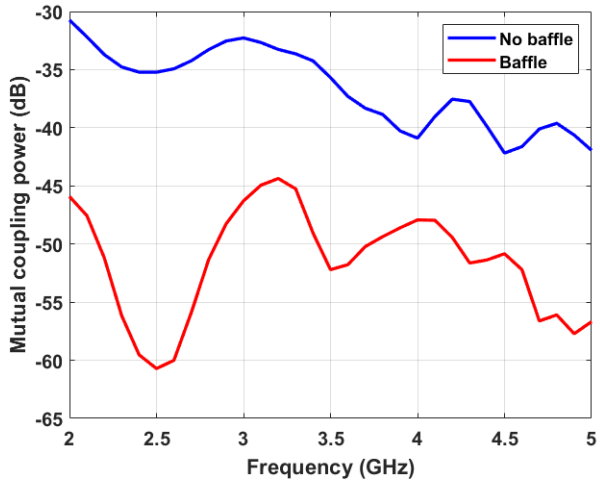

Figure 5.11: Simulated mutual coupling power between two SH-2000 horn antennas with and without a baffle in FEKO

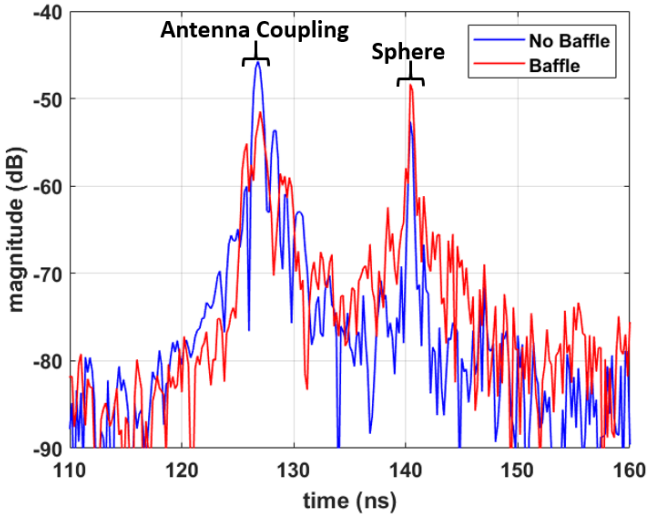

Figure 5.12: The matched filter output after background subtraction for a 3-inch sphere measured from 2-5 GHz with and without a baffle

quality results in this scenario.

5.3.2 Time-Gating Window Selection

In some measurement spaces, it is not possible to sufficiently separate the OUT from nearby scatterers. For example, in the small chamber setup shown in Fig.

5.13, there is a metal plate beneath the foam on the azimuthal positioner directly behind the OUT. Measurements taken in this configuration are used to study window selection to suppress nearby clutter.

To begin, the effects of the rectangular window's width are studied, and results are compared in Fig. 5.14. An excessively wide window includes surrounding clutter, and oscillations occur, as seen in the "Wide" trace. When the window is too narrow, it does not fully capture the return from one of the spheres due to their separation in time, as previously discussed in Section 3.2. This uneven attenuation causes an almost constant offset in the measured RCS, as shown in the "Narrow" trace. When the window is wide enough to surround the entirety of both sphere returns without including extraneous clutter, the "Best" scenario is achieved. However, the processing is still not optimal because the rectangular window shape adds oscillations to the results [22].

Fig. 5.15a shows the results of applying rectangle and Hanning windows of the

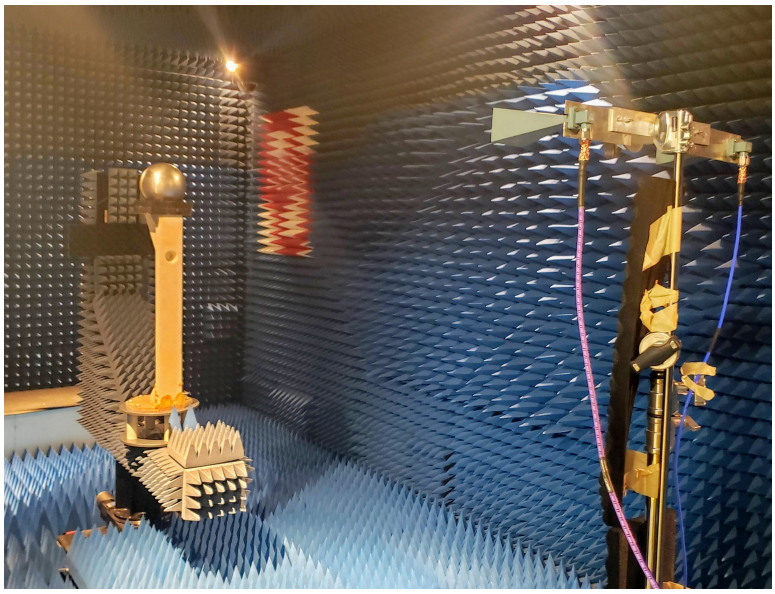

Figure 5.13: Small anechoic chamber test setup

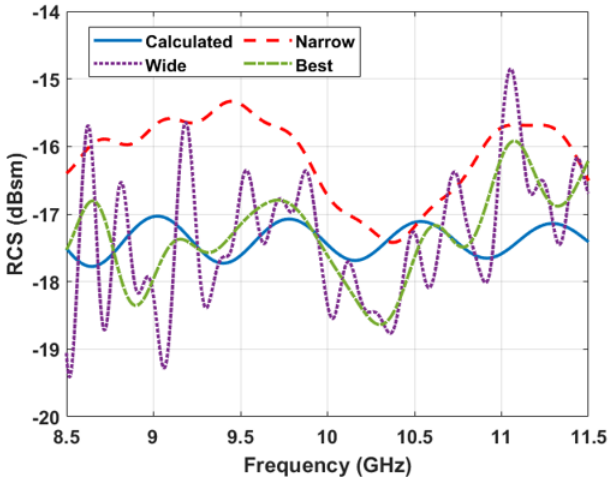

Figure 5.14: Measured RCS of a 6-inch sphere after calibration with a 12-inch sphere using different time gating window widths compared to analytically calculated values

same width. The Hanning window does not produce the large oscillations seen in the rectangular window results. However, there is a large offset between the measured and theoretical RCS because the tapered window applies different weights to the sphere returns. Therefore, the width of a tapered window must be wider to accommodate the returns arriving at different times. The alternative is to use a

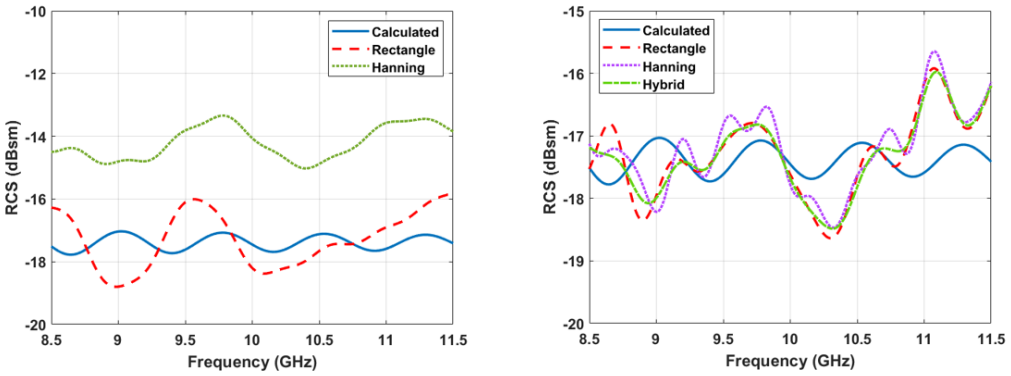

(a) Same Width

(b) Optimized Widths

Figure 5.15: Measured RCS of a 6-inch sphere after calibration with a 12-inch sphere using different time gating window shapes of the same width in (a) and their respective optimized widths in (b), both compared to analytically calculated values

hybrid window, which is the convolution of a Hanning and rectangular window as described in Section 3.2. To effectively compare each window shape's potential, each shape's width is optimized to minimize the average error, and the three optimized windows are shown in Fig. 5.16. The corresponding RCS values are shown in Fig. 5.15b. Because these measurements were taken in a smaller anechoic chamber, the multi-path reflections are not attenuated as much by free-space path loss as in the large anechoic chamber. Additionally, some of the sidelobes from the large return of the positioner overlap with the OUT's return. Background subtraction and time-gating partially mitigate these issues, but none of the window shapes can remove this clutter completely. However, applying the hybrid window does reduce the average error by 74% from 8.5-11.5 GHz compared to measurements with no time-gating.

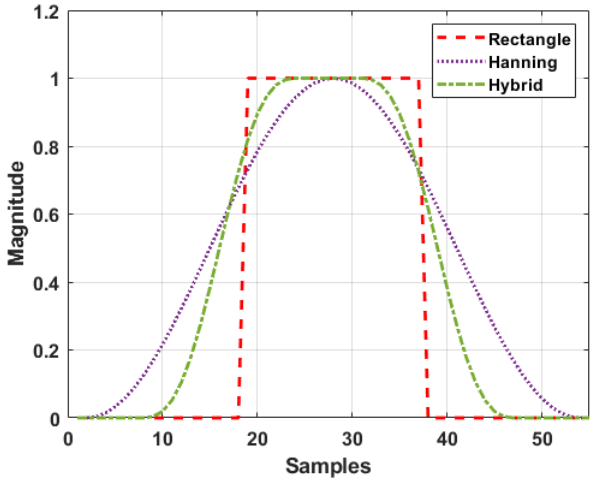

Figure 5.16: Three shapes of windows used for time-gating with their respective optimized widths

5.4 Measurement Parameter Choice

Selecting the proper measurement settings is equally as important as using appropriate test setup hardware. A coupler near the transmit antenna is sometimes used as the reference transmit signal in chamber S_{21} measurements to compensate for the cables' losses. Because some post-processing is done in the time domain, the reference signals should truly be the power transmitted and power received. Using a coupler path as a reference leads to inaccuracies in the time domain analysis. Temporal errors are also introduced when the OUT lies beyond the maximum unambiguous range (R_{max}) set by the frequency step size, as discussed in Section 3.1. If clutter lies beyond R_{max}, it folds into the first range swath, potentially overlapping with the OUT. As a result, selecting an R_{max} value that is well beyond the OUT ensures that distant clutter remains well-separated from the desired return. Eventually, this distant clutter is attenuated by the chamber walls and free-space path loss, and the subsequent return is insignificant. In this work, the back wall of the chamber produces the last substantial return, and the R_{max} value is selected to exceed the distance to the back wall. There is an estimated 20 m of RF cable with a relative permittivity approximately equal to 2 and 13.6 m of total free-space propagation. Applying these parameters to (3.8), the maximum step size allowed for this measurement setup is 3.58 MHz. A frequency step size of 2 MHz is chosen to ensure that the OUT is well-separated from multi-path reflections.

Extra bandwidth above and below the frequencies of interest is measured and truncated at the end of post processing to mitigate edge effects inherent to Fourier analysis. This increased bandwidth also improves temporal resolution, increasing the ability to separate the OUT from surrounding clutter. Alternatively, if measuring a wide bandwidth is not possible, a hybrid window is applied instead of a

rectangular window during time-gating, as described in Section 3.2.

The final measurement parameter to consider is the intermediate frequency (IF) bandpass filter bandwidth of the VNA's receivers. Selecting the IF bandwidth is a tradeoff between reducing the noise allowed into the measurement as described in (3.10) and increasing the measurement time. The IF bandwidth and measurement time are inversely proportional, so decreasing the IF bandwidth by a factor of 10 increases the measurement time by a factor of 10. The effect of IF bandwidth on subsequent RCS measurement values is depicted in Fig. 5.17, and the corresponding error values are given in Table 5.1. There is not as much change across the IF

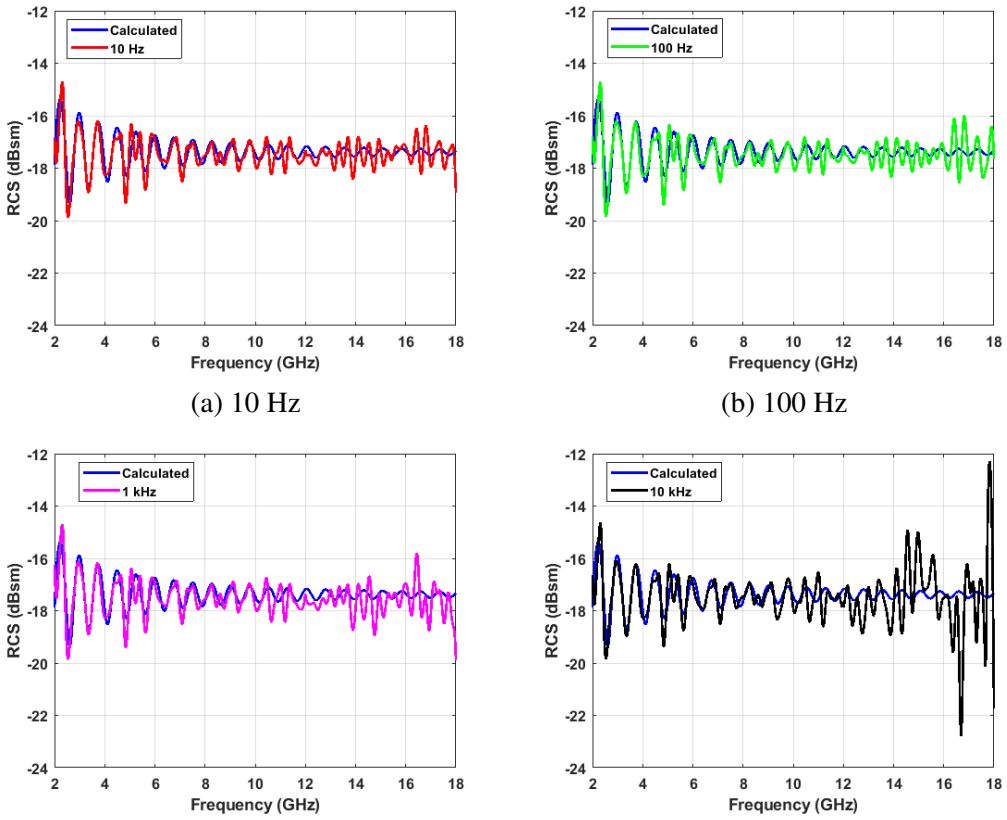

(a) 10 Hz

(b) 100 Hz

(c) 1 kHz

(d) 10 kHz

Figure 5.17: The RCS of a 6-inch sphere calibrated with a 12-inch sphere measured using different IF bandwidths

bandwidth settings when measuring from 2-8 GHz. However, the error increases significantly at the higher frequencies as the IF bandwidth increases. This work uses a 10 Hz IF bandwidth to achieve high accuracy over a large bandwidth.

5.5 Measurement Across Angle

In some cases, RCS may need to be known as a function of azimuthal angle. To do so, the OUT is placed on a rotary pedestal, and the pedestal is coordinated with the VNA to rotate after each frequency sweep. The test time is the product of the desired number of frequency points, the number of angles, and the time for a single angle measurement. Therefore, it is desirable to use software to automate the coordination between the VNA and rotary pedestal. In this work, the Spectrum 959 software controls the instrumentation.

Another factor to consider when measuring over multiple angles is the azimuthal symmetry of the setup. If the setup is perfectly symmetric, only one empty chamber measurement and one calibration set measurement are necessary for the calibration process. In this work, the foam support structure is symmetric, but fins and metal hardware on the bottom of the rotational pedestal vary across angles. Therefore, the empty chamber must be measured for each angle and subtracted from each corresponding OUT angle measurement. However, the elements within

Frequency Range (GHz)	IF Bandwidth			
	10 Hz	100 Hz	1 kHz	10 kHz
2-8	0.343	0.348	0.339	0.351
12-18	0.314	0.380	0.463	0.984
2-18	0.309	0.335	0.372	0.579

Table 5.1: The average error values in dBsm across three different frequency ranges for various IF bandwidths

the calibration set, like cable loss and amplifier gain, remain constant over angle, so it is hypothesized that a single calibration set may be used for all of the angles.

If a single empty chamber measurement were needed, the test time would be significantly reduced. For this reason, a study is conducted to verify the assumption that an empty chamber measurement is necessary for each angle. When the empty measurement and 6-inch sphere measurement are collected at the same angle, there is an initial peak in the time domain from the antenna coupling and a second, larger peak corresponding to the sphere's return, as shown in Fig. 5.18a. The subsequent sphere RCS values in Fig. 5.18b align very well with the theoretical values. On the other hand, using an empty measurement collected at a 90° azimuthal offset from the sphere measurement leads to much more noise in the time domain, as seen in Fig. 5.18c. As a result, the corresponding measured RCS in Fig. 5.18d has a wider variation and is much less accurate. In conclusion, in this test configuration, matching the angle of the collected empty chamber measurement to the OUT measurement angle is essential for accurate results.

As discussed in Section 2.3, the sphere is a common calibration object because its RCS does not depend on angle. Until the sphere's electrical circumference is well into the optical scattering region, the RCS varies over frequency. Measurement across angle should theoretically be flat assuming the sphere is perfectly spherical, which is true in this case because the calibration spheres are made with 0.0003 sphericity, which describes the error between the surface area of the manufactured shape and a perfect sphere [31]. The results of measuring a 6-inch sphere over angle using a single calibration set and angle-dependent empty chamber measurements are shown in Fig. 5.19. At each of the frequencies, the measured RCS across angle is flat within a fraction of one dBsm, indicating that adding azimuthal rotation does not significantly diminish the measurement accuracy.

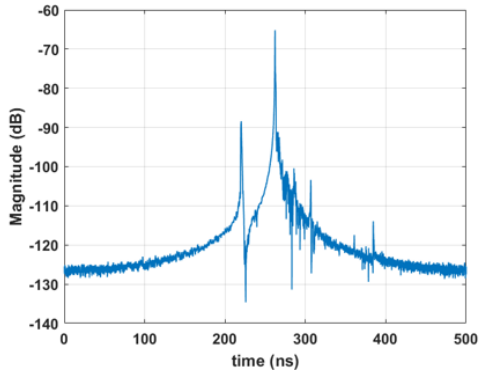

(a) Matched angles (time domain)

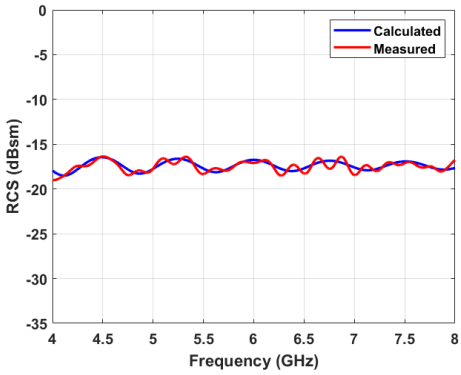

(b) Matched angles (frequency domain)

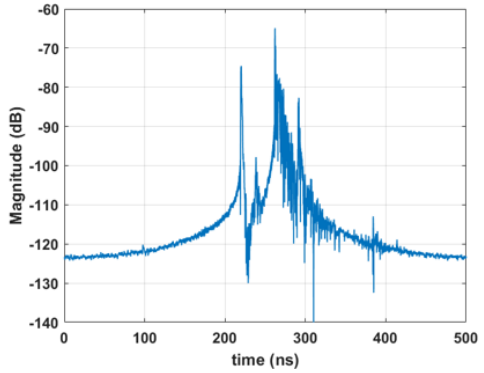

(c) 90° mismatch (time domain)

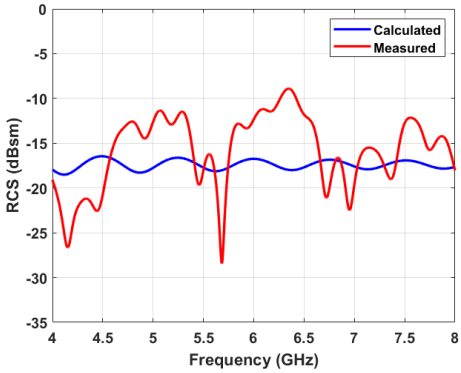

(d) 90° mismatch (frequency domain)

Figure 5.18: Comparison of time domain and susbequent measured RCS values compared to analytically calculated values when the same angle is used for the sphere and background measurement and when there is a 90° mismatch in angle

5.6 Distributed Measurements

While all of the techniques discussed above are straightforward for a single point target OUT, measuring distributed objects is much more complex. The multiple scattering sources cover a more extensive range swath, so a wider window is required, which lets in more clutter. Unlike a single sphere that produces a neatly defined peak well above the clutter, determining exactly where the desired OUT return ends and clutter begins is more challenging. Additionally, the complex interactions with constructive and destructive interference between the points of scatter-

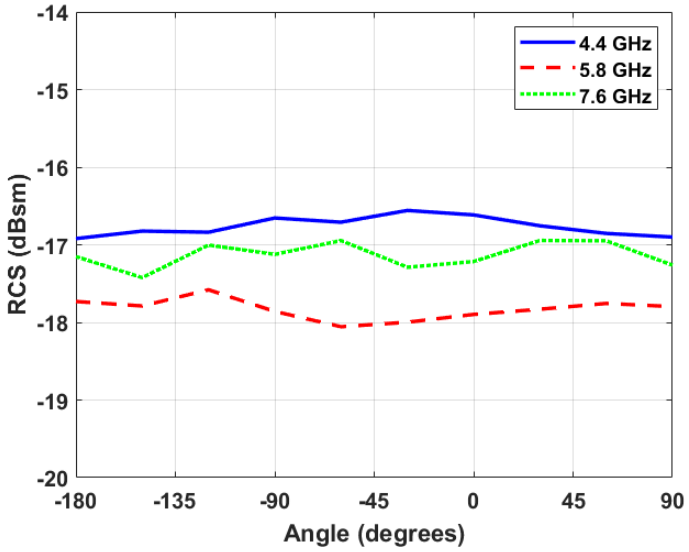

Figure 5.19: The measured RCS of a 6-inch sphere calibrated with a 12-inch sphere measured across angle at different frequencies [4]

ing can make the RCS more sensitive to angle. Because of this complicated RCS behavior, statistical models, as opposed to deterministic models, are often used to represent the RCS of objects in practice [23].

5.6.1 Spheres

A distributed OUT is comprised of four 5-inch spheres and arranged as seen in Fig. 5.20. When one sphere is measured, there is one primary peak from the specular return and one secondary peak from the creeping wave. When four spheres are measured, the distributed peak produces several peaks of various magnitudes in the time domain, as seen in Fig. 5.21. Instead of yielding one specular response and one creeping wave response for each sphere, one sphere's reflection interacts with another [32]. This multi-bounce scattering leads to a broader range of RCS values because both constructive and destructive interference occurs. This phenomena is the primary difference between several single points targets in close proximity and

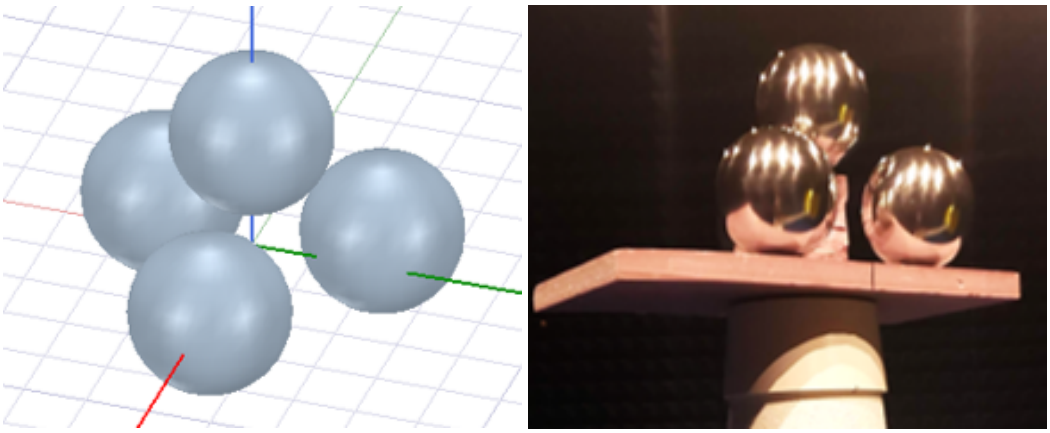

(a) FEKO (b) Measured

Figure 5.20: Configuration of 5-inch spheres for distributed simulations in FEKO and in measurements

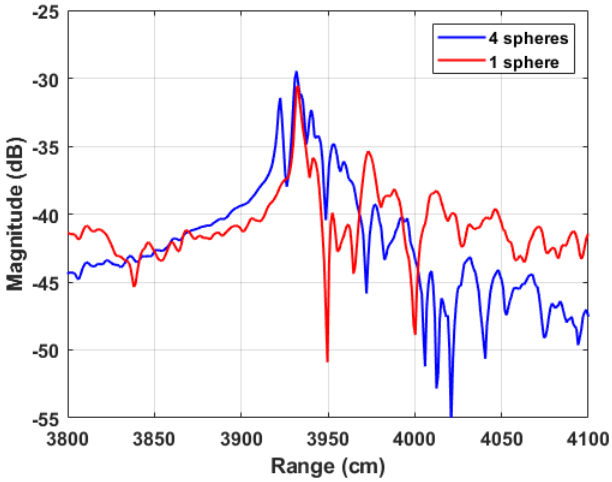

Figure 5.21: Measured RCS of four 5-inch spheres compared to one 6-inch sphere

a distributed target. The interactions of all the single points target returns within a distributed target interact in such a way that the overall response is altered.

The sphere geometry is simulated in FEKO and compared to measured results, as shown in Fig. 5.22. Because of these complex interactions, the RCS is sensitive to the exact spacing of the spheres. The slight frequency offset and magnitude deviation are due to the spheres' slight misalignments in the fabricated prototype

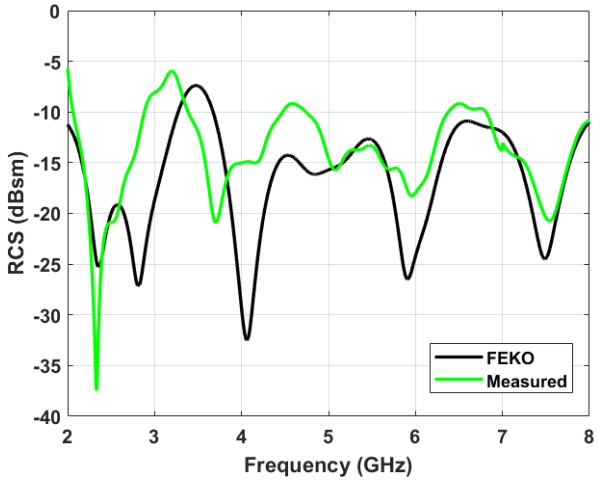

Figure 5.22: Measured and simulated RCS of four 5-inch spheres

and z-axis alignment of the prototype with the antennas. Furthermore, the spheres purchased for these measurements are not constructed for electromagnetic measurements (i.e. they are not entirely spherical). First of all, the bottom is flattened with a keyhole cutout for mounting. Additionally, their material does not have the same conductivity properties as the aluminum in simulation. The measured RCS of the spheres from 2-18 GHz is shown in Fig. 5.23. The pattern of peaks and nulls con-

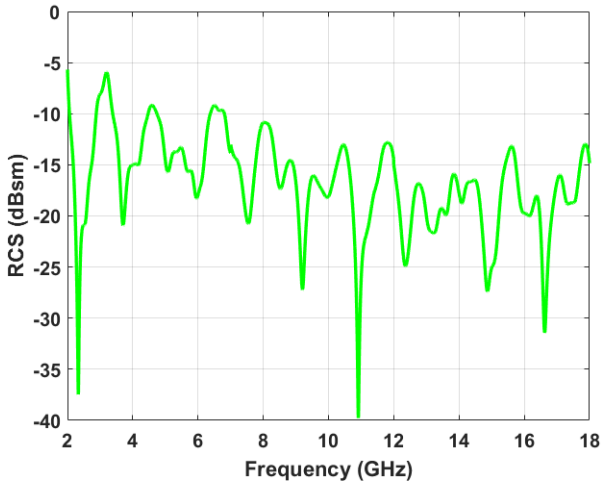

Figure 5.23: Measured RCS of four 5-inch spheres

tinues throughout the frequency range, though the average magnitude of the RCS decreases with frequency. As the scattering off of the spheres becomes more specular at higher frequencies, the effect of one sphere shadowing another becomes more prominent, and the subsequent RCS is decreased. Moreover, the spacing between the spheres appears electrically larger at higher frequencies, causing the geometry to appear rougher. A larger electrical spacing lowers the amplitude of the fields that reflect off of multiple surfaces before scattering back to the antennas [33].

5.6.2 UAV Measurements

Now that the overall RCS extraction, signal processing algorithms, and simulations have been verified for single point targets and simple distributed targets, a more complex distributed target can be measured with high degree of confidence in the resultant measured RCS. The OU Skywalker UAV is measured from 2-18 GHz over angle with vertical and horizontal polarizations. As introduced in Section 4.3, simulating the entire UAV body is not feasible. Instead, the UAV is modeled only with its carbon fiber rods, which are required to attach the wings to the body, and an aluminum motor. The validity of this simplification is further analyzed later in this section.

Initially, the RCS of the UAV with vertical and horizontal propeller rotations is compared to determine whether separate measurements are needed for different propeller rotations, and the results are seen in Fig. 5.24. It is evident that the propeller's position does not have a significant impact on the overall RCS of the UAV. This result is expected because the propeller is plastic and curved such that there is minimal broadside reflection. For consistency across future analysis, the UAV is measured with a vertically-rotated propeller.

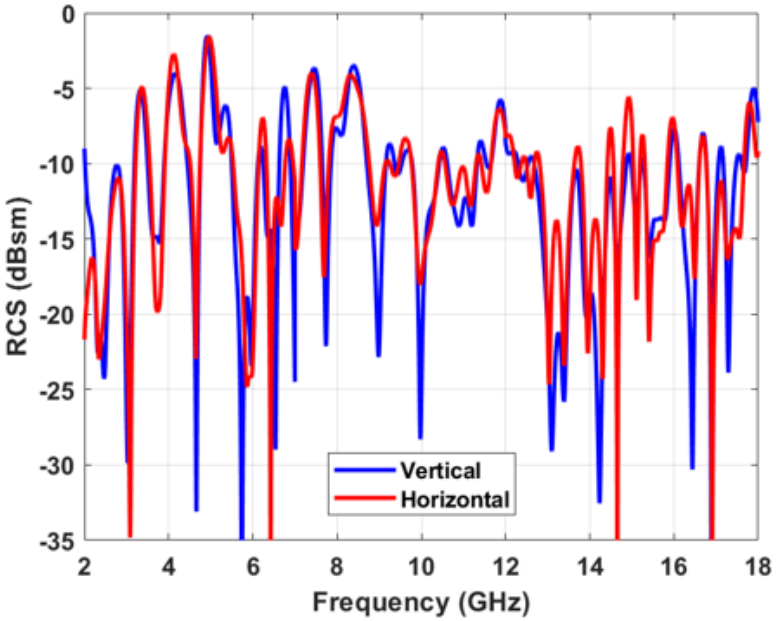

Figure 5.24: Measured RCS of the OU Skywalker with its propeller rotated vertically and horizontally

Next, the individual contributions from the components are analyzed by taking measurements of just the carbon fiber rods and of the rods and motor, spaced at the same intervals as the objects sitting within the UAV, as shown in Fig. 5.25. Fig.

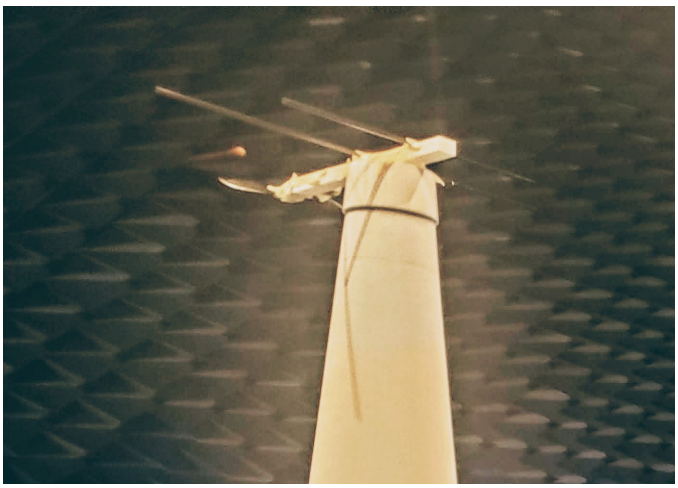

Figure 5.25: Measurement configuration of carbon fiber rods, aluminum motor, and plastic propeller

5.26 shows the measured RCS values. Initially, the large oscillatory variance of the UAV RCS across frequency is surprising after focusing on spheres, which have a much more consistent RCS, for the majority of this work. Comparing the isolated components with the entire UAV reveals that the rods' unique response dominates the overall response. Adding in the motor interferes slightly and shifts the peaks and troughs of the response, and the addition of the remaining wires and components inside the UAV further interferes with the rods' response. The oscillation in the rod RCS is due to constructive and destructive interference between the incident wave's reflection off of the two rods. When the rod spacing is an even integer multiple of the incident wavelength divided by two, a maximum occurs. Conversely, a minimum occurs when the rod spacing corresponds to an odd integer multiple of the incident wavelength divided by four. Overall, identifying the source of the RCS oscillations verifies that the full UAV measurement results are reasonable.

Fig. 5.27 further explores the components' RCS contributions by illustrating

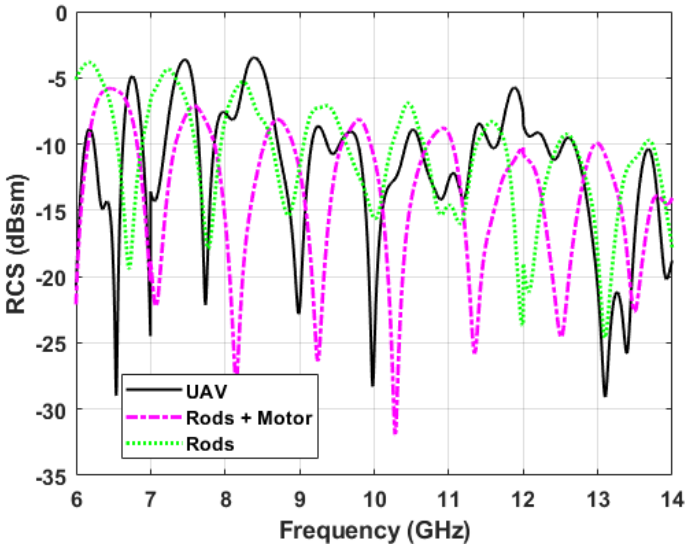

Figure 5.26: Measured RCS of the carbon fiber rods, rods with motor and propeller, and entire UAV

the background-subtracted measurements in the time domain. This perspective emphasizes the powerful return from the rods, with a secondary contribution from the motor, which time align very well with the large return signals from the full UAV measurement. The returns from the other components in the full UAV are minor and vary because fixed-wing UAVs are highly customizable.

There is no default carbon fiber material in FEKO, so a custom material must be defined. The electrical properties of carbon fiber can vary widely with frequency and with the polymer composition, with relative permittivity ranging from 5 to 29 and conductivity ranging from 10^{-13} S/m to $100,000$ S/m [34] [35] [36]. Fig. 5.28 demonstrates that the initial simulation results of the carbon fiber rods have a similar shape to the measurement of the rods taken out of the full UAV, but the magnitude and spacing of the peaks do not line up. Changing the conductivity and permittivity of the carbon fiber material in FEKO did not have much of an effect on the resulting RCS over the studied frequency range because most of the scattering is in the optical

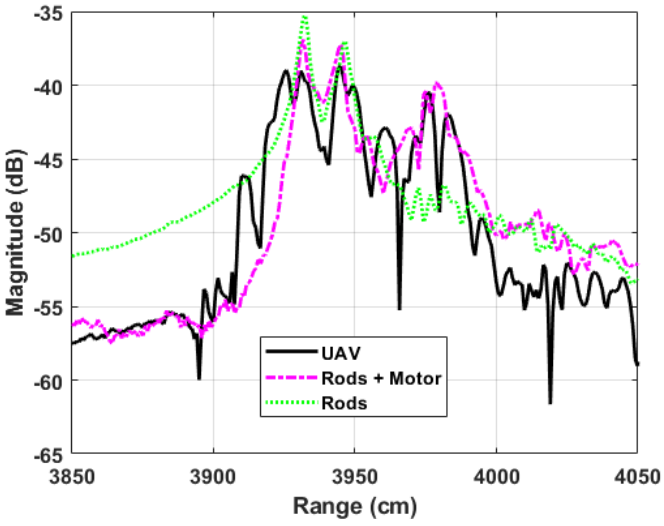

Figure 5.27: Time domain return from the carbon fiber rods, rods with motor and propeller, and entire UAV measured from 6-14 GHz

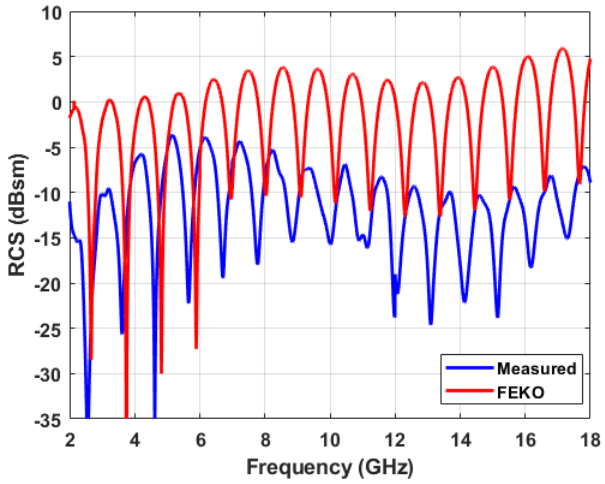

Figure 5.28: Measured RCS of carbon fiber rods compared to FEKO simulation

region where reflection rather than radiation is the primary scattering mechanism. The permittivity of the carbon fiber is different from air, so a reflection occurs when the wave is incident upon this permittivity change.

Further investigation revealed that geometry differences have a much larger effect on the RCS than changes to the material properties. This behavior is expected because the shape of the rods is similar to the wire discussed in Section 2.4. The wire's RCS decreases quickly within a few degrees of normal incidence. One cause of geometry discrepancy is the chamber's azimuthal positioner. This positioner rotates 1° after placing the OUT but before the measurements begin. Furthermore, ensuring a precise and accurate alignment within a fraction of a degree within this setup is generally difficult due to the 6.8 m distance from the antennas and OUT.

When the simulated incident wave is rotated azimuthally by 1.5°, the measured RCS aligns much better with the simulation, as seen in Fig. 5.29. The measured and simulated rods and motor are compared in Fig. 5.30. The measurement follows the same upward trend as the simulation at the lower frequency but does not reach as high of a magnitude at the higher frequencies. Differences in the measured and

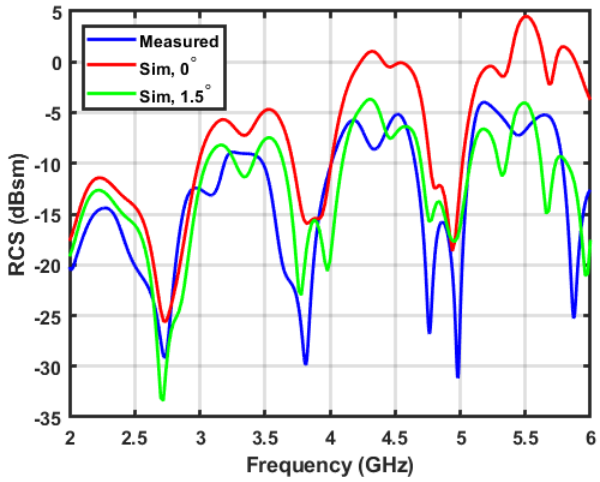

Figure 5.29: Simulated RCS of rods and motor with a head-on incident wave and an incident wave rotated 1.5° azimuthally compared to measured rods and motor RCS

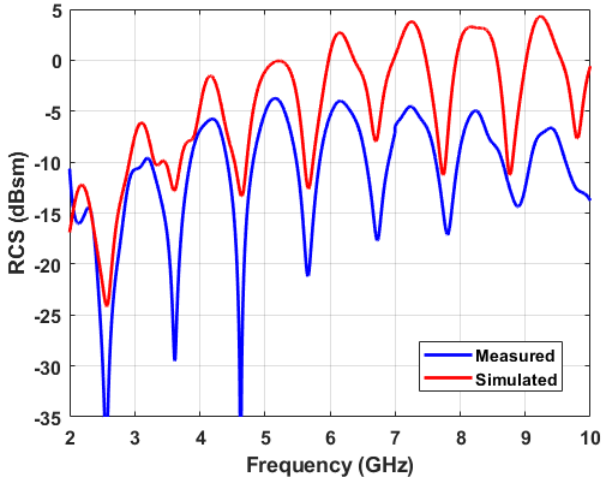

Figure 5.30: Measured RCS of rods and motor with vertical polarization compared to FEKO simulation

simulated magnitude and location of RCS peaks are seen throughout this work due to the sensitivity in azimuthal alignment. The challenge of accurately modeling the carbon fiber in the rods contributes to the remaining error. The rods' electrical properties cannot be directly measured, and the weaving of the fibers is difficult to model accurately.

To evaluate the simplification of representing the UAV by just the rods and motor, the simulation of the rods and motor is compared to the measurement of the full UAV, and the results are seen in Fig. 5.31. The additional components add some other fluctuations in RCS and reduce the overall UAV RCS because of the added interference (diffuse scattering). However, the overall shape is still similar to the simulated rods and motor. Because the measurement of just the rods and motor aligned well with simulation, the discrepancy between the measured UAV and simulated rods and motor is not from measurement error. The rods and motor do not effectively represent the full UAV, and the simulation model must be improved for better alignment between measurement and simulation.

Finally, the UAV's RCS across angle is analyzed. Figure 5.32 depicts the UAV from several incident angles, where 0° corresponds to the wave incident on the UAV's nose. For the vertical polarization, RCS is consistently smallest when the incident wave is at a 42° angle. This result is as expected because there are no broadside specular reflections from any of the components at this angle. For the horizontal polarization, the largest return occurs when observing the UAV head-on

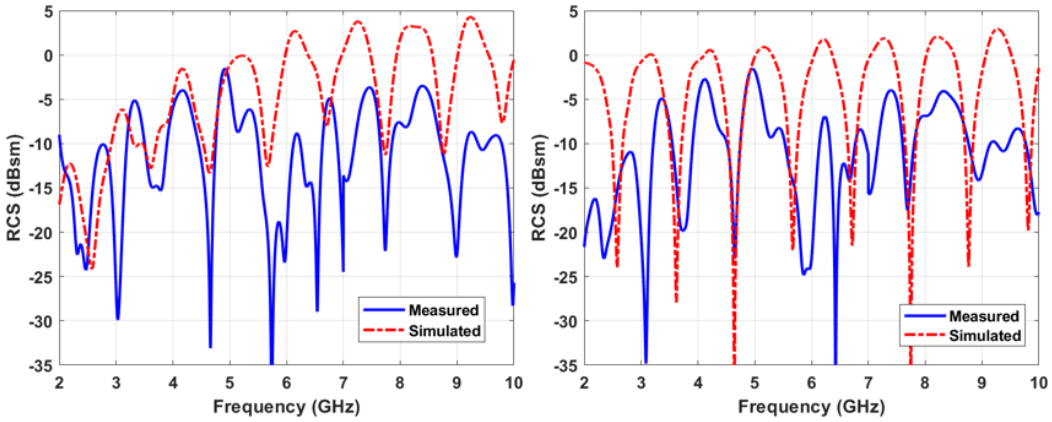

(a) Vertical polarization (b) Horizontal polarization

Figure 5.31: Simulated rods and motor RCS and measured UAV RCS with different polarizations

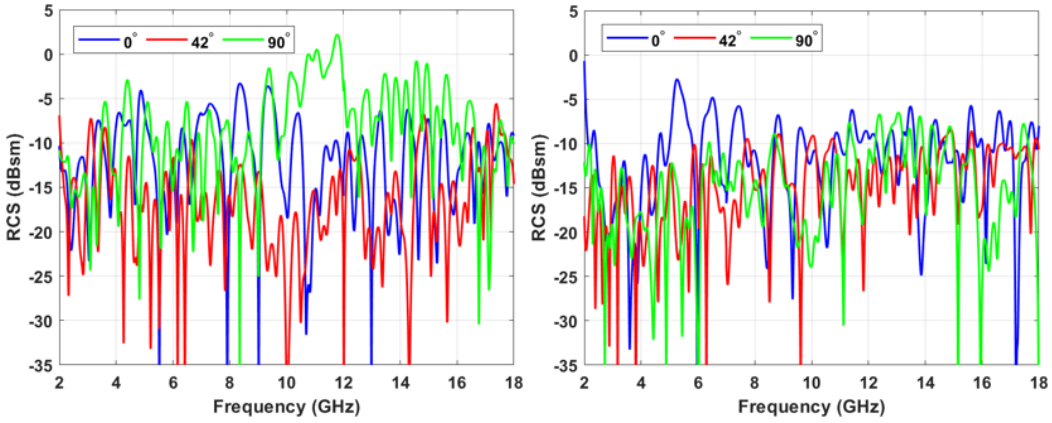

(a) Vertical Polarization (b) Horizontal polarization

Figure 5.32: Measured UAV RCS with different incident plane wave angles

similar to the vertical polarization. The two measurement polarizations are directly compared for head-on and side UAV measurements in Fig. 5.33. For the head-on measurements in Fig. 5.33a, the RCS is not consistently larger for either of the polarizations. At most frequencies, if the RCS is at a minimum in one polarization, the RCS in the other polarization is at a maximum. A radar measuring both polarizations could take advantage of this observation to maximize its ability to detect the UAV. For measurements of the UAV's side, as seen in Fig. 5.33b, the RCS viewed

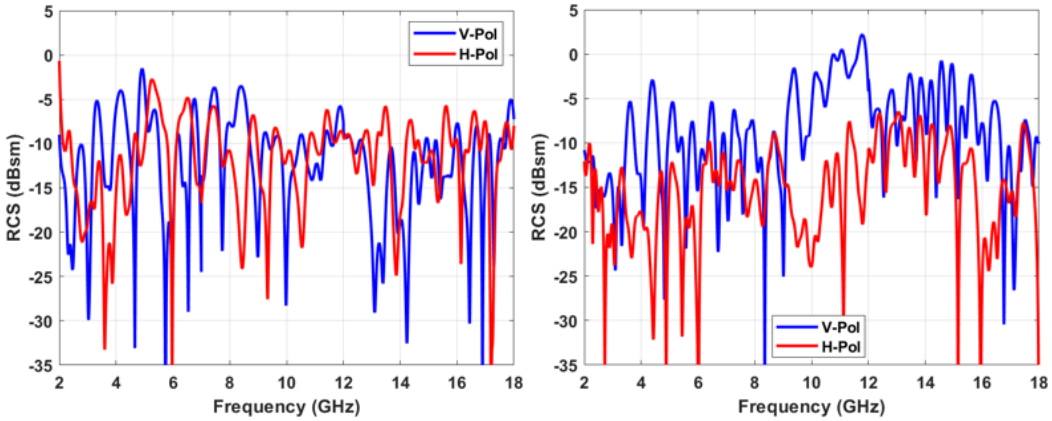

(a) Head on (b) Side

Figure 5.33: RCS of UAV measured with vertical and horizontal polarization

with a vertically polarized wave is consistently equal to or greater than the horizontal polarization. At this angle, the rods' contribution is expected to be similar for both polarizations because their circular ends are facing the antennas. Therefore the primary difference is expected to be from the additional UAV components. For example, there is a 2.4 GHz dielectric antenna near the front of the UAV that points upward that backscatters more energy from a vertically polarized wave than a horizontally polarized wave.

The UAV is then measured at 61 azimuthal angles across $360°$, and the results are shown in Fig. 5.34. For both polarizations, the RCS has a strong dependency on angle. The angles of maxima and minima are not consistent between the two frequencies. To evaluate the validity of the FEKO model simplification across azimuthal angle, the rods and motor are simulated with the incident wave geometry shown in Fig. 5.35a. The rods and motor simulation's RCS peaks at incident angles of $0°$ and $180°$, and the magnitude rapidly falls off after a few degrees of rotation, as shown in Fig. 5.36. As a result, correct alignment is crucial for comparing values. The simulated RCS oscillates rapidly across angle, so some features may be missed

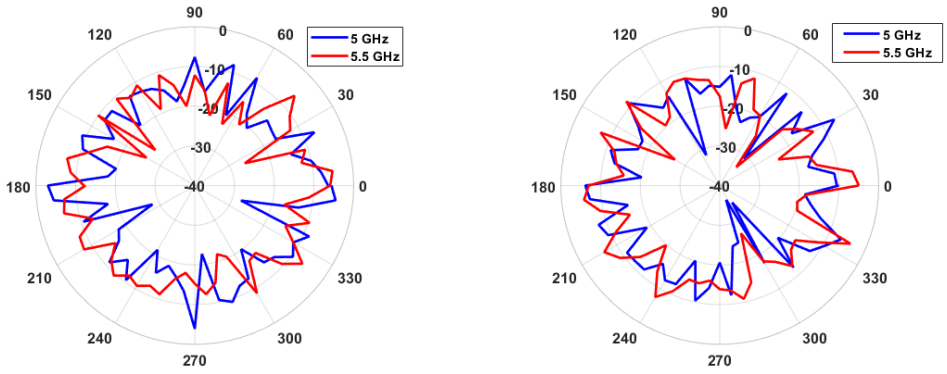

(a) Vertical Polarization

(b) Horizontal polarization

Figure 5.34: Measured UAV RCS across azimuthal angle at different frequencies and polarizations

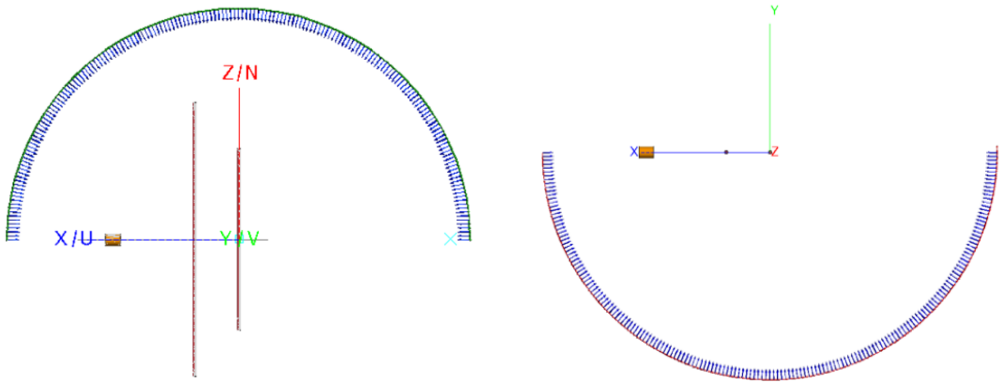

(a) Azimuth (b) Elevation

Figure 5.35: FEKO geometry for simulating RCS across angle

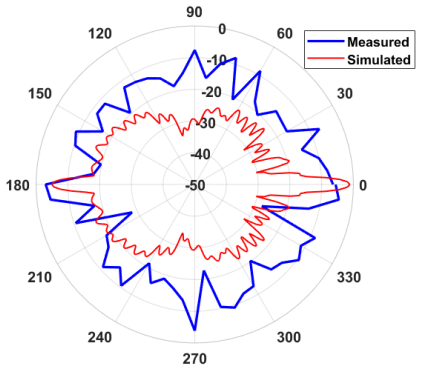

(a) 5 GHz, Vertical Polarization

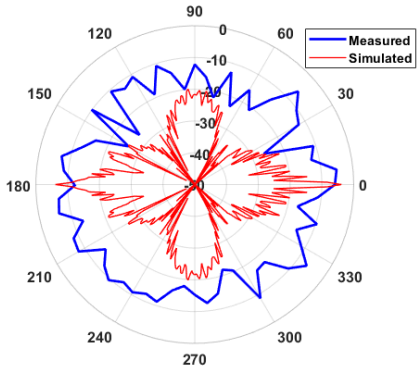

(b) 5.5 GHz, Vertical Polarization

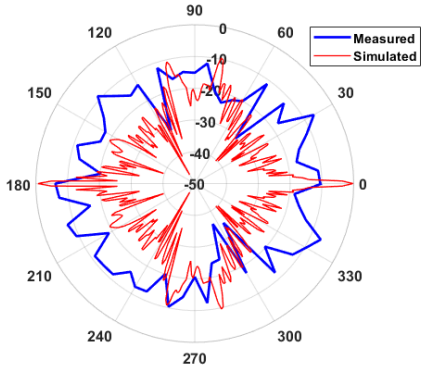

(c) 5 GHz, Horizontal Polarization

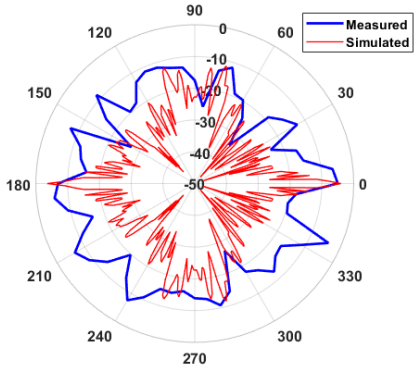

(d) 5.5 GHz, HorizontalPolarization

Figure 5.36: Measured UAV RCS across azimuthal angle compared to simulated rods and motor in FEKO

with the coarse 6° measurement angle step size. In general, the measured RCS is larger than the simulated RCS when viewing the UAV from angles off of broadside. While earlier analysis showed that the rods and motor are the dominant scatterers within the UAV at broadside, Section 2.4 indicates that the rods' RCS quickly decreases with even a few degrees of azimuthal rotation. As a result, the UAV's RCS is only approximately equal to the RCS of the rods and motor at broadside. More components of the UAV must be added to the simulation to model the RCS at other incident angles effectively.

Next, the UAV scattering is analyzed as a function of elevation angle to find the RCS of the UAV when it is above the antennas. First, Fig. 5.35b depicts the incident wave angle sweep to simulate the rods and motor in FEKO. Fig. 5.37 shows the simulation results, where 0° corresponds to the UAV's nose. The RCS varies greatly across elevation angle; however, the horizontal polarization consistently produces a larger backscatter because it creates a stronger dipole moment along the length of the carbon fiber rods, as discussed in Section 2.1.1. The RCS with horizontal polarization peaks at the back of the UAV where the larger rod is closer to the

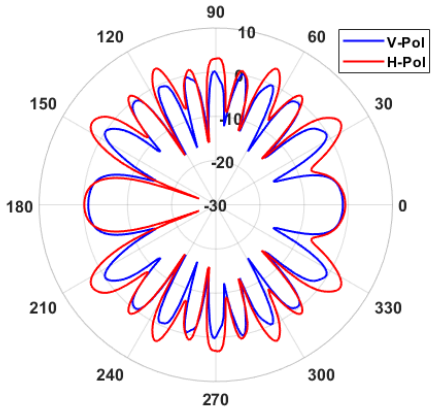

Figure 5.37: RCS of rods and motor across elevation angle with vertical and horizontal elevation simulated in FEKO at 5 GHz

antennas, thus creating an even larger dipole moment.

It is difficult to measure the UAV across elevation with the same angular resolution as the azimuthal measurements. For this reason, this work only includes a 90° elevation angle measurement, as seen in Fig. 5.38. The rods and motor are measured individually to determine their contribution to the overall RCS, and Fig. 5.39 compares the results. The average RCS magnitude is similar across the three measurements, but the added components in the UAV add other oscillations. To analyze how well the simulated rods and motor align with the actual rods and motor when viewed from the underside, the measured and simulated rods and motor RCS are compared in Fig. 5.40. While the oscillations' depth and location don't align precisely, the general upward trend of the magnitude aligns between the simulation and measurement.

Next, the model's validity is verified by comparing the simulated rods and motor to the full UAV RCS, as shown in Fig. 5.41. Both scenarios yield an RCS that has many peaks and valleys across frequency. However, the simulation has a general

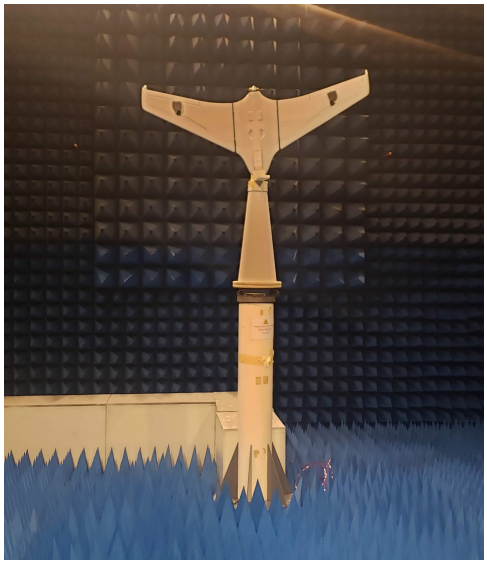

Figure 5.38: Mounting configuration for measuring underside of UAV

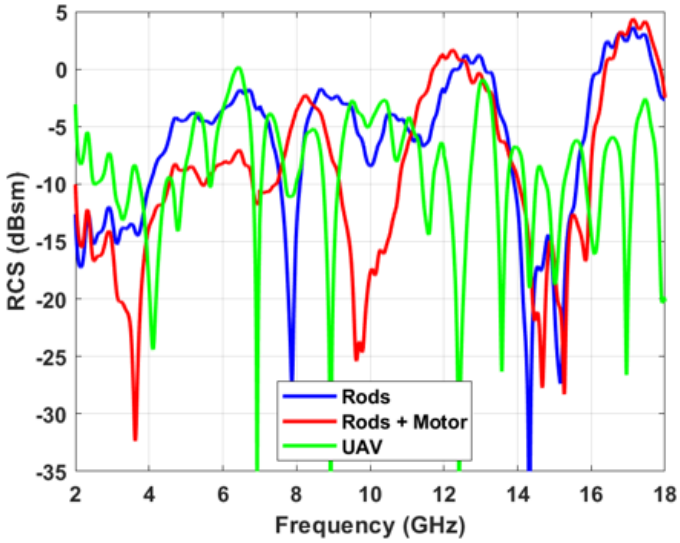

Figure 5.39: Measurements of rods, rods and motor, and full UAV at a 90° elevation rotation

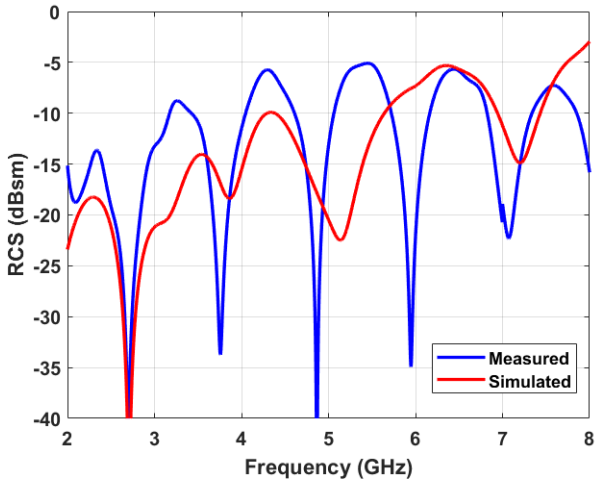

Figure 5.40: Comparison of measured and simulated carbon fiber rods and aluminum motor at a 90° elevation rotation

upward trend while the measurement's average level remains relatively constant. Overall, the simulated rods and motor do not agree as well with the measured UAV at this elevation angle as they do across azimuthal angle. This discrepancy is because the large surface area of foam broadside to the antennas and additional components within the UAV contribute substantially to the overall backscatter. More-

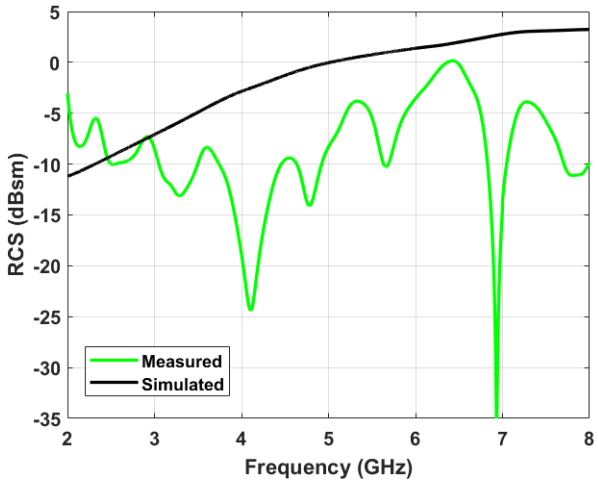

Figure 5.41: Measurement of UAV and FEKO simulation of the carbon fiber rods and motor

over, in this scenario, the UAV truly behaves as a distributed target rather than a few individual scatterers. It is more difficult to accurately extract the RCS of a truly distributed target without waveform optimization or more complex signal processing techniques because the time-domain response is more than a few separable peaks. Furthermore, these results indicate that the additional components within the UAV and the foam frame that were omitted initially due to computational limitations must be considered to create an accurate simulation model.

Chapter 6

Low Frequency

In this chapter, the measurement setup discussed in Chapter 5 is adapted for single antenna measurements from 100 MHz to 2 GHz. Using two antennas is not practical for measuring RCS below 2 GHz in the anechoic chamber at the University of Oklahoma. Even if two antennas that operate in the desired frequency range were available, the physical size of low-frequency antennas creates challenges. Mounting two large, heavy antennas in an anechoic chamber is difficult, and maintaining a quasi-monostatic configuration is complicated due to the larger separation between the antennas' phase centers. Instead, this chapter proposes using measured reflection coefficient results from a single antenna to extract RCS. This setup is more affordable than traditional chamber setups because it only requires a generic VNA and rotary pedestal capable of communicating with National Instruments (NI) LabVIEW software, and it is portable enough to be used for outdoor measurements. Single antenna RCS measurements have been published before at 10 GHz, but they lack automation, portability, and quantitative error analysis [37].

6.1 Indoor Measurement Configuration

The same SFCW radar principles previously discussed, such as range resolution and maximum unambiguous range, apply to this setup, except the reflection coefficient S_{11} is used in place of S_{21} for the value of $\frac{P_r}{P_t}$. OU master's student Rylee Mattingly developed an NI LabVIEW program to coordinate and automate the instrumentation. The graphical user interface for controlling the frequency and angle of the measurements is shown in Fig. 6.1. The NI LabVIEW program is interfaced with the rest of the setup as illustrated in Fig. 6.2. A handheld N9917A Keysight FieldFox in VNA mode and a Microwave Vision Group SH200 dual ridge horn antenna are used to collect measurements. An Aerotech rotary stage with a Soloist motion controller is used to rotate the OUT azimuthally. An L-com RF shielded ethernet cable transmits and receives data between the laptop and the instrumen-

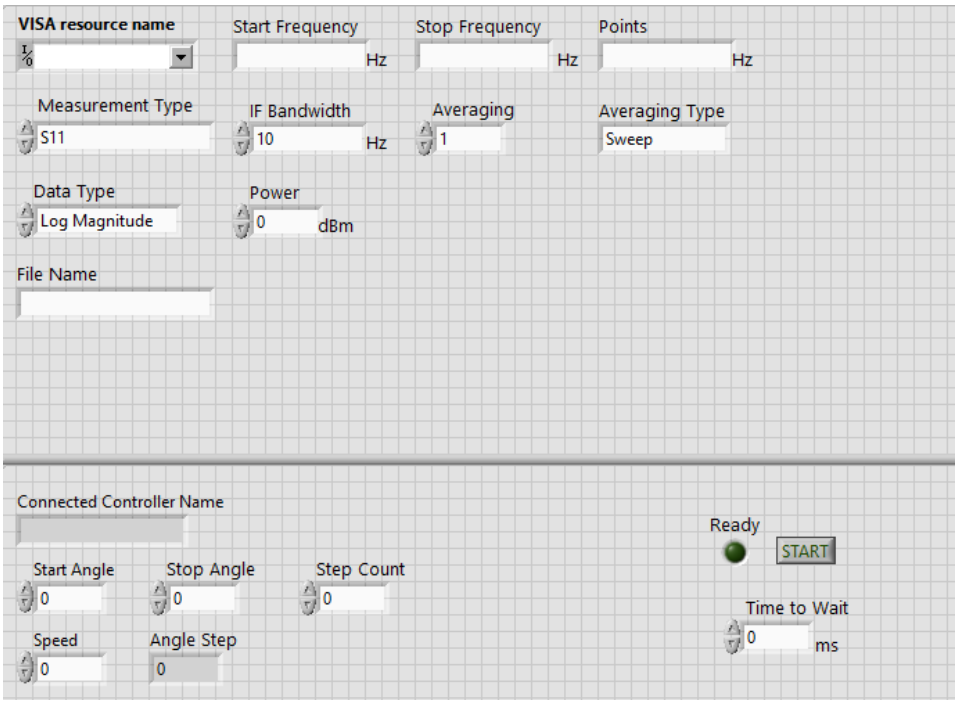

Figure 6.1: LabVIEW GUI for single-antenna measurements

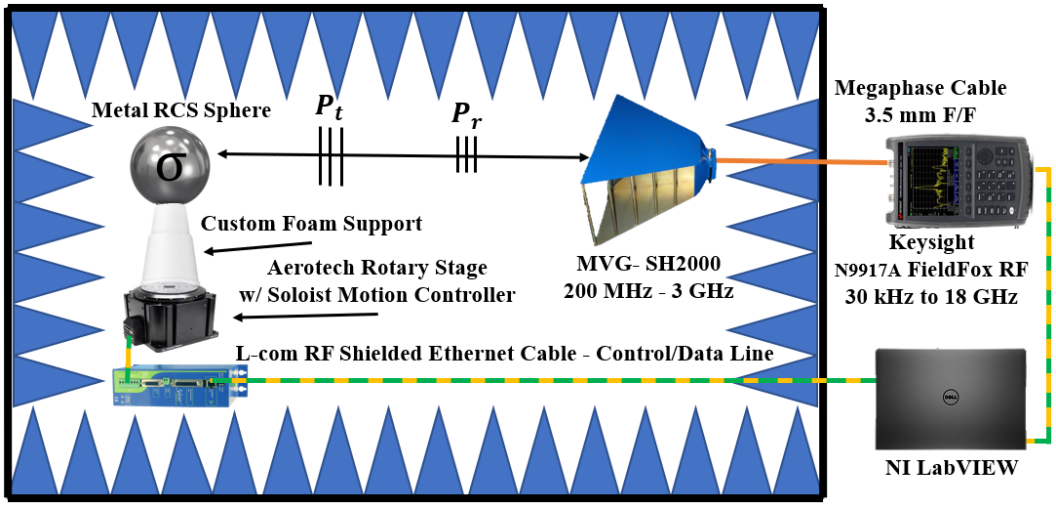

Figure 6.2: Block diagram of anechoic chamber test setup

tation, and the truncated cone support structure described in Chapter 5 holds the OUT. Fig. 6.3 shows the complete test setup.

This setup introduces new challenges not seen in the two-antenna setup discussed in Chapter 5. Because of the bi-directional signal travel between the Field-

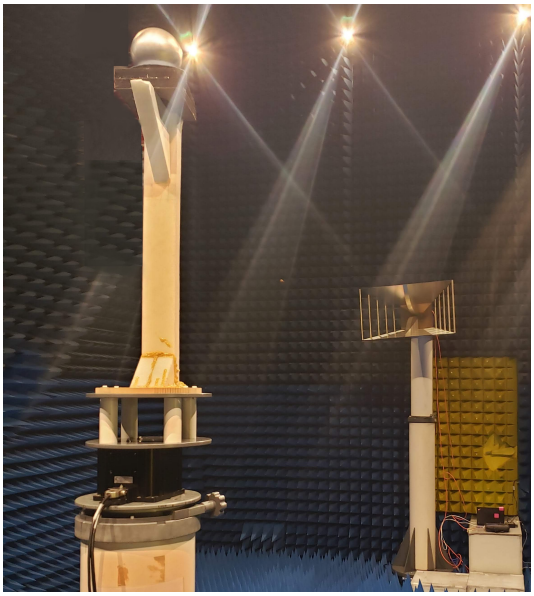

Figure 6.3: Antenna and OUT configuration within anechoic chamber for single-antenna backscatter measurements

Fox and the antenna, an amplifier cannot be added to improve SNR without also adding a circulator. Moreover, the stepper motor is only a few feet away from the OUT instead being at the bottom of the pedestal below the chamber foam. Furthermore, even though the setup's Ethernet cable is shielded, there is still more communication between instrumentation occurring out in the open in the chamber than in the two-antenna setup. Lastly, the foam absorbers lining the chamber walls have a decreased ability to absorb incident waves at lower frequencies, so there is an increase in multi-path reflections. On the other hand, the system losses are lower. Frequency-dependent spherical spreading loss and RF cable loss decrease with frequency. A shorter length of RF cable connects the antenna and FieldFox as opposed to the cable connecting the antennas and the VNA in the two-antenna configuration.

6.2 Results

Before background subtraction, the most prominent feature in this measurement configuration's range profile, depicted in the "Raw" trace in Fig. 6.4, is centered around 50 ns. This time corresponds to the time it takes for the wave to propagate from the FieldFox through the RF cable to the antenna's port and back through the RF cable to the FieldFox. After vector background subtraction, the return from the OUT appears at 90 ns. Without background subtraction, the limited chamber dynamic range completely buries the OUT's return below the noise floor. Thus, this step is essential to obtain meaningful results with this measurement configuration.

Even though the ethernet cables running between the laptop and the instrumentation are shielded, they do not entirely contain all digital signals, which is seen as a rise in the noise floor of the measured data compared to previous re-

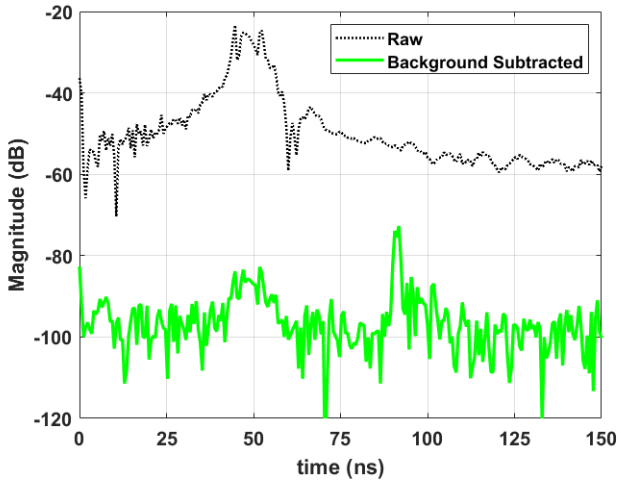

Figure 6.4: The matched filter output from a 6-inch sphere measured from 200-1200 MHz with and without vector background subtraction

sults. Measurements of a 6-inch sphere are repeated twice with the two-antenna configuration described in Chapter 5, and Fig. 6.5a shows the power after background subtraction. There are some differences between the two measurements due to imperfections in the background subtraction; however, they generally follow the same trend. For the single-antenna configuration, the background-subtracted measurements in Fig. 6.5b do not agree with each other above 1.5 GHz, meaning that the background-subtracted measurements' performance is not consistent across repeated trials. The narrow peaks at specific frequencies that vary in magnitude between different rounds of measurements are from high-frequency digital signals that radiate from the long cables and instrumentation. While the cables are shielded, discontinuities such as connectors and long cables are great radiators. Moreover, the data traveling along the cables vary in time, so the radiated signal during the "background" measurement is not the same as the radiated signal during the "OUT" measurement. Background subtraction is unable to remove this inconsistent digital noise. For this reason, UHF-band (0.3-1 GHz) results are the focus

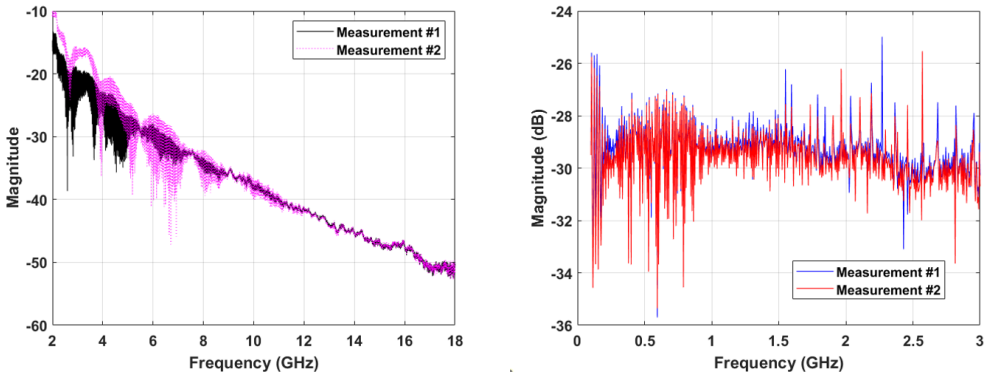

(a) Two Antennas (b) Single Antenna

Figure 6.5: Background subtracted measurements of a 6-inch sphere collected with one and two antenna configurations

of the remainder of the analysis.

After background subtraction and applying the calibration set, the subsequent measured RCS shown in Fig. 6.6 is centered around the correct values, but a significant variance is present. In addition to the challenges of substantial loss in RF cables and multi-path reflections overcome in Chapter 5, the single antenna config-

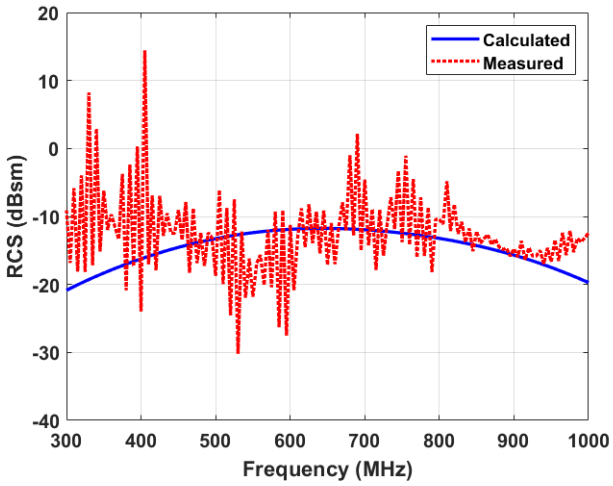

Figure 6.6: The measured RCS of a 6-inch sphere calibrated with a 12-inch sphere after background subtraction with no time-gating compared to analytically calculated values

uration adds additional obstacles. The rotary stage is a large metal scatterer close to the OUT, and the antenna mismatch reflection spans a longer duration than the antenna coupling in the two-antenna setup. To remove the clutter without introducing unwanted edge effects, a hybrid window created by convolving a Hanning window with a rectangular window is applied in post-processing to time-gate around the OUT return, and the results are seen in Fig. 6.7. Before time-gating, the average error is 4.9 dBsm. After time-gating, the error is reduced to only 0.36 dBsm because the hybrid window removes the majority of the surrounding clutter without distorting the edges of the frequency range.

The UAV is then measured using both vertical and horizontal polarization, and the results are compared to simulations in Fig. 6.8. Some differences between the measured and simulated values are because the simulation only includes the rods and motor. However, there is a significant disparity, especially with the vertical polarization. Fig. 6.9 compares the measurements in the time domain. The return from the sphere and the UAV measured with vertical polarization begin at 1350 cm.

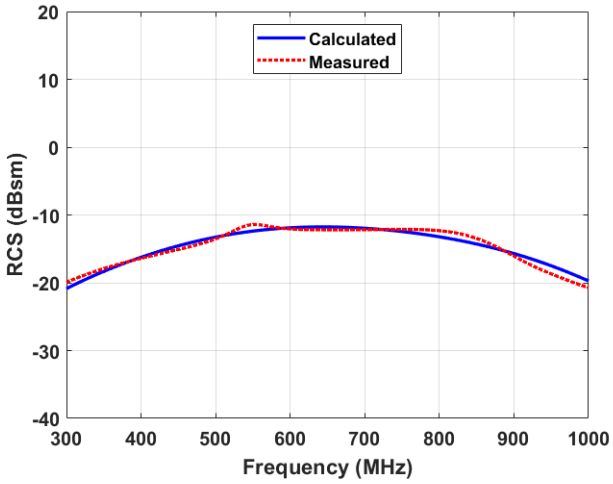

Figure 6.7: The measured RCS of a 6-inch sphere calibrated with a 12-inch sphere after background subtraction and time-gating compared to analytically calculated values

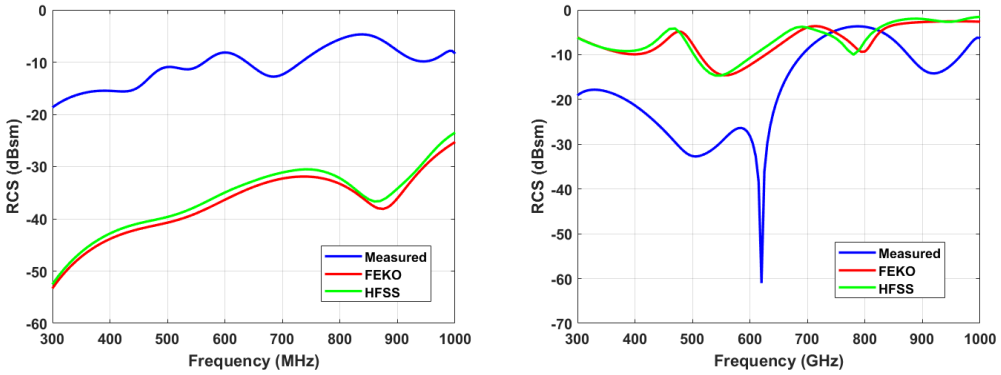

(a) Vertical Polarization (b) Horizontal Polarization

Figure 6.8: The measured RCS of the UAV compared to FEKO and HFSS simulations of the carbon fiber rods and aluminum motor

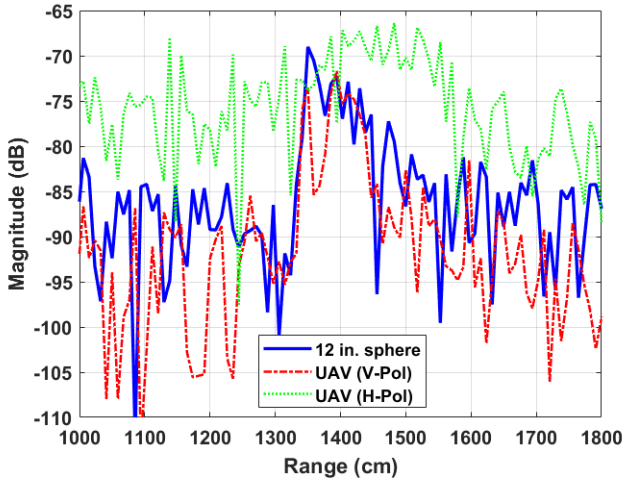

Figure 6.9: Time-domain measurement after background subtraction

The rotary pedestal's return arrives shortly after the OUT return, and the sidelobes from the two returns may overlap; thus, this is why the measured RCS is much higher than simulated RCS since the measured is a combination of both the UAV and the pedestal. The noise floor of the UAV measurement with horizontal polarization is higher than the vertical polarization, and there is no defined start or end of the OUT return. The separation in time between the empty chamber and OUT measurements is greater for the horizontal polarization than the vertical polarization. This

temporal separation reduces the coherency of the background subtraction, reducing this technique's ability to suppress the clutter.

Because of the current measurement configuration's limited accuracy, the UAV's rods and motor are simulated to gain insight on features to focus future redesign efforts. Polarization plays a prominent role in the RCS magnitude, as seen in Fig. 6.10. The lower-frequency incident wave is in the Rayleigh scattering region, as discussed in Section 2.1. Therefore the dipole moment induced along the rod's length by the horizontally-polarized wave is much larger than the dipole moment induced along the rod's diameter by the vertically-polarized wave. There is an additional phenomenon acting at the lower frequencies. Because the rods are somewhat conductive, standing waves form along the length of the rods, and peaks in the radiated field occur when each rod is a half-wavelength long. It appears that the rods are acting like half-wave dipole antennas [38]. The first peak at 155 MHz is from the 889 mm rod, and the second peak at 224 MHz is from the 590 mm rod. The effective dielectric constant (ε_r) of the carbon fiber rods can be derived from the

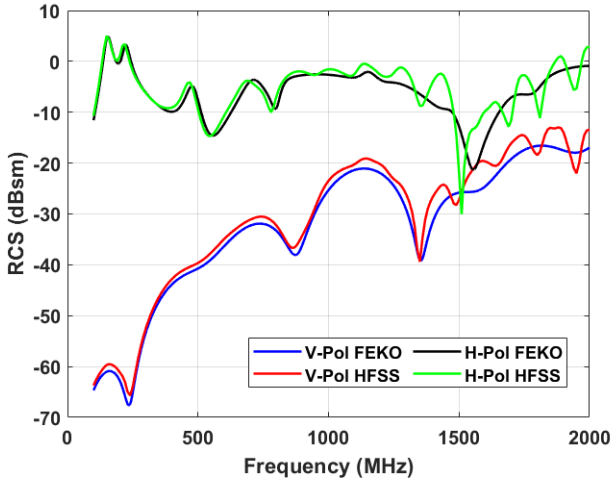

Figure 6.10: Simulated carbon fiber rods and aluminum motor RCS in HFSS and FEKO with vertical and horizontal polarization

peak frequencies (f) as

$$\frac{\lambda}{2} = \frac{c}{2f\sqrt{\varepsilon_r}} = L \tag{6.1}$$

where L is the length of the rod and λ is the wavelength within the dielectric. The first frequency yields $\varepsilon_r = 1.19$. This permittivity is then used to solve for the resonant frequency of the second rod. The resultant calculated frequency of 233 MHz is very close to the simulated second peak at 224 MHz. The difference in these values is due to interactions between the two rods. To further analyze the scattering at the first resonant frequency, the rods and motor are simulated over azimuth and elevation angle at the two peak frequencies, and the results are shown in Fig. 6.11. The front rod is broadside at $90°$, and the motor points to $270°$. The almost-isotropic pattern with nulls at endfire in Fig. 6.11a and the almost-uniform pattern in Fig. 6.11b identically resemble a dipole antenna's radiation pattern. Overall, it has been shown that the carbon fiber rods behave like half-wave dipoles for low-frequency horizontally-polarized excitations.

To further improve the measurement accuracy, the SNR can be improved by reducing the distance between the antenna and the OUT as long as the far-field

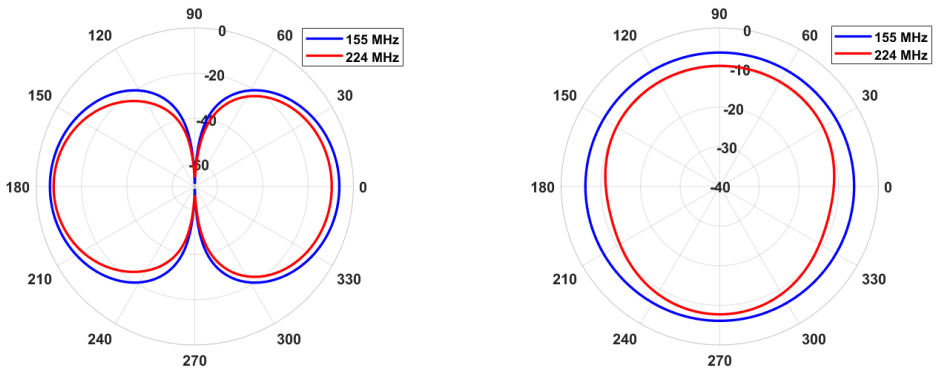

(a) Azimuth (b) Elevation

Figure 6.11: The measured RCS of the UAV compared to FEKO and HFSS simulations of the carbon fiber rods and aluminum motor

criterion in Section 3.3 is still satisfied. Additionally, increasing the transmit power would raise the desired signal farther above the thermal noise floor. This setup's frequency range capabilities could be expanded by more effectively suppressing the digital noise by adding shielding around the instrumentation.

6.3 Outdoor Measurements

To demonstrate the portability and flexibility of the single antenna configuration, measurements are collected outdoors, as shown in Fig. 6.12. The range between the antenna and the OUT may be easily adjusted in this setup because the antenna is on a mobile cart. Unlike the anechoic chamber setup, ground bounce must be taken into account in the outdoor configuration. Ground bounce occurs when the signal travels from the antenna to the ground to the OUT before being reflected back to the ground and then to the antenna. If possible, the measurement range is selected to maintain the far-field criterion while also minimizing the amount of the antenna beamwidth that reaches the ground.

Figure 6.12: Outdoor single-antenna measurement configuration

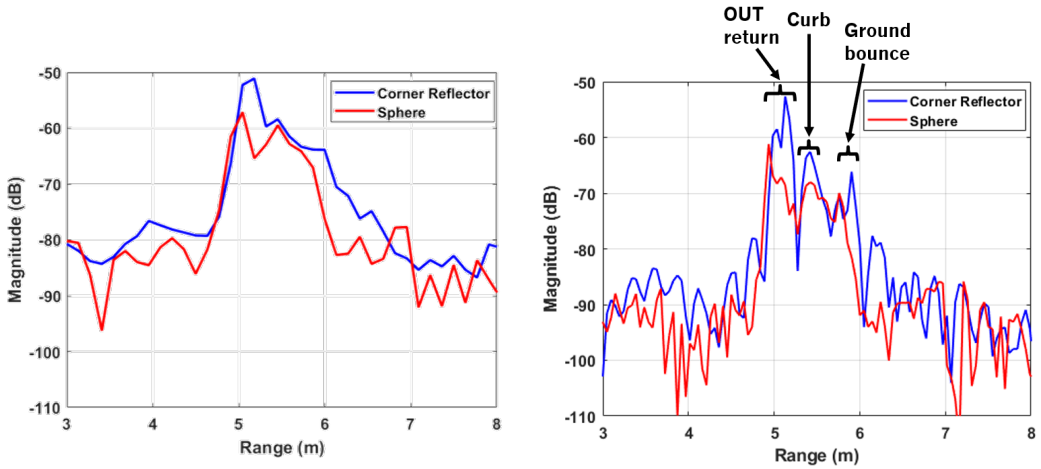

(a) 100-1100 MHz (b) 100-3100 MHz

Figure 6.13: Background-subtracted outdoor measurements in the time domain

Selecting the bandwidth to process is a trade-off between temporal resolution and inclusion of electromagnetic interference from over-the-air communications. When only 1 GHz of bandwidth is used, the OUT return is indistinguishable from the clutter, as seen in Fig. 6.13a. With a 3 GHz bandwidth, separate returns from the OUT, curb, and ground bounce can be distinguished, as shown in Fig. 6.13b. Vector background subtraction does not remove ground bounce because this multi-path reflection only occurs when the OUT is present. As a result, both background subtraction and time-gating are necessary to remove the clutter. A hybrid window created by convolving rectangular and Hanning windows is used to fully capture the returns from the calibration sphere and corner reflector. The measured RCS of the corner reflector after background-subtraction and time-gating is shown in Fig. 6.14. Processing a 1.6 GHz bandwidth yields an average error of 12.2% or 0.551 dBsm. This level of accuracy is sufficient for many applications; however, the error can be further reduced by taking measurements in an anechoic chamber or by reducing the ground bounce. Ground bounce is minimized by raising the antenna and OUT

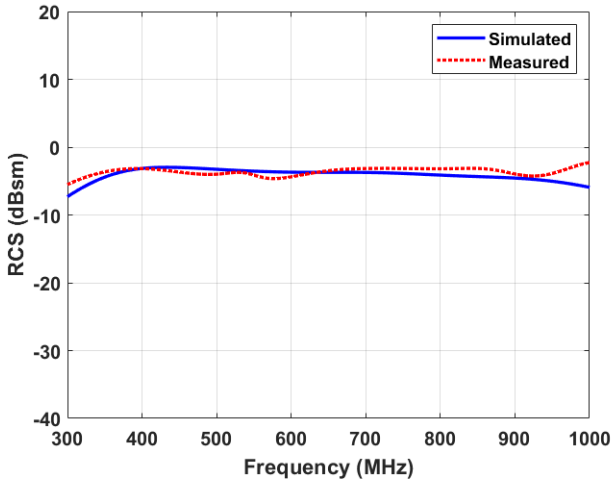

Figure 6.14: The measured RCS of a 13.5-inch corner reflector calibrated with a 12-inch sphere compared to analytically calculated values

farther off of the ground or by adding scatterers in the ground bounce path to reduce the amount of energy reflected back in the direction of the antenna.

Chapter 7

Conclusions and Future Work

An RCS measurement methodology has been designed and executed for measurement across frequency and azimuthal angle. By implementing the time-gating methods described in this thesis, the error in the measured 6-inch sphere RCS is reduced by 62% from 2-18 GHz. After making a few hardware upgrades to reduce clutter and increase the signal-to-noise ratio, the total error reduction is 74%. Overall, this thesis details RCS extraction techniques that yield highly accurate results over an ultra-wide bandwidth, with an average error below 5% or 0.21 dBsm from 2-18 GHz. These measurement principles are adapted to complete measurements below 2 GHz by leveraging single-antenna reflection coefficient values. A flexible test configuration using LabVIEW achieves an average error of 0.54 dBsm from 300-1000 MHz.

After complete verification of RCS extraction using spheres, the derived RCS methodology was applied to the OU Skywalker UAV. The UAV's overall RCS contains large oscillations across frequency. After analyzing the contributions from individual components in the frequency and time domain, the carbon fiber rods and aluminum motor are identified as the dominant scatterers within the UAV. In particular, the constructive and destructive interference between the two rods causes the oscillations in RCS. In addition to varying with frequency, the UAV's RCS also

depends on the incident wave's polarization. One polarization does not consistently measure a higher RCS than the other from 2-18 GHz. Below 2 GHz, the RCS is much higher when the incident wave polarization is parallel to the carbon fiber rods. The UAV's RCS also changes rapidly across angle, with the largest reflections occurring when the wave is incident upon the UAV's nose and tail.

There are several areas of future research related to improving the flexibility and accuracy of this work. Strategic hardware selection and post-processing algorithms overcame many clutter challenges in the anechoic chamber. However, more error is introduced in sub-optimal measurement environments. For example, in the Advanced Radar Research Center's near-field chamber, seen in Fig. 5.13, a foam-covered metal positioner is in close proximity to the OUT. The residual clutter after background subtraction overlaps in time with the sphere return, as shown in Fig. 7.1, so the clutter cannot be removed entirely with time-gating. More sophisticated processing can be applied to separate the desired return from large scatterers nearby. Adaptive pulse compression can extract the return from a small object masked by the sidelobes of other returns, increasing the potential for measurement accuracy in challenging environments [39] [40].

Minor hardware adaptations are necessary to expand the measurement frequency capabilities. A different amplifier is necessary to measure above 18 GHz. In addition to a higher frequency of operation, the amplifier needs to be more powerful to offset the increase in losses. The measurements below 2 GHz can be improved with better digital noise shielding and reducing the distance between the antenna and the OUT. A circulator could be utilized to add an amplifier despite the bi-directional signal travel along the RF cable. The measurements would need to be broken up in smaller frequency groups because each circulator can only support a relatively narrow bandwidth.

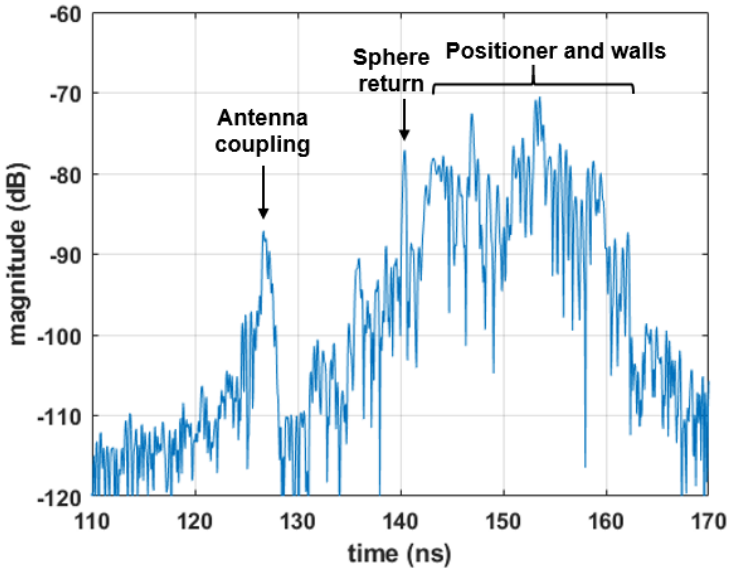

Figure 7.1: The matched filter output after background subtraction for a 3-inch sphere measured from 12-16 GHz

Finally, the UAV's RCS characterization can be refined. Re-measuring the UAV with finer azimuthal resolution will ensure that all RCS features are captured. Designing a structure to support the UAV while measuring across elevation angle will allow more angular information to be collected. The UAV simulation model needs to be improved because the rods and motor do not accurately represent the full UAV at angles off of broadside due to the larger surface area of foam resulting in a larger and more complex distributed target. If the radar utilizes both vertical and horizontal polarization (a polarimetric radar), the signal after matched filtering is affected by the object's RCS at both polarizations. Averaging measurements from both polarizations together would provide more insight into detection of the object from a polarimetric radar. Additionally, the measurement process can be applied to different UAV models and other objects of interest.

References

[1] E. F. Knott, *Radar cross section*, 2nd ed., ser. SciTech radar and defense series. Raleigh, NC: SciTech Pub., 2004.

[2] M. T. Tavis, "Radar cross section of thin wires at all angles of incidence," *Journal of applied physics*, vol. 45, no. 3, pp. 1179–1182, 1974.

[3] Azizah, A. B. Suksmono, and A. Munir, "Signal processing of range detection for sfcw radars using matlab and gnu radio," in *2014 International Conference on Computer, Control, Informatics and Its Applications (IC3INA)*, 2014, pp. 145–148.

[4] R. E. Jarvis, J. G. Metcalf, J. E. Ruyle, and J. W. McDaniel, "Measurement and signal processing techniques for extracting highly accurate and wideband rcs," *Accepted to the 2021 IEEE International Instrumentation and Measurement Technology Conference*, 2021.

[5] D. Jenn, *Radar and Laser Cross Section Engineering, Second Edition*, 2nd ed., ser. AIAA education series. Washington, DC: American Institute of Aeronautics and Astronautics, Inc, 2005.

[6] R. B. Dybdal, "Radar cross section measurements," *Proceedings of the IEEE*, vol. 75, no. 4, pp. 498–516, 1987.

[7] D. L. Mensa, "Wideband radar cross section diagnostic measurements," *IEEE Transactions on Instrumentation and Measurement*, vol. 33, no. 3, pp. 206–214, 1984.

[8] D. K. D. K. Cheng, *Field and wave electromagnetics / David K. Cheng.*, 2nd ed., ser. Addison-Wesley series in electrical engineering. Reading, Mass.: Addison-Wesley, 1990.

[9] L. B. Felsen and N. Marcuvitz, *Radiation and Scattering of Waves*, 1994.

[10] A. Ishimaru, *Electromagnetic Wave Propagation, Radiation, and Scattering: From Fundamentals to Applications*, 2nd ed., ser. IEEE Press Series on Electromagnetic Wave Theory. New York: Wiley, 2017.

[11] E. P. Lavin, *Specular reflection*, ser. Monographs on applied optics; no. 2. New York: American Elsevier Pub. Co., 1971.

[12] "IEEE recommended practice for radar cross-section test procedures," *IEEE Std 1502-2007*, pp. 1–70, 2007.

[13] C. A. Balanis, *Advanced engineering electromagnetics*, 2nd ed. Hoboken, N.J.: John Wiley & Sons, 2012.

[14] D. Long and F. T. Ulaby, *Microwave Radar And Radiometric Remote Sensing*, ser. Artech House Microwave Remote Sensing series. Artech House, 2015.

[15] J. A. Stratton, *Electromagnetic theory by Julius Adams Stratton.*, ser. IEEE Press series on electromagnetic wave theory. Piscataway, NJ: IEEE Press, 2007.

[16] M. Abramowitz, *Handbook of mathematical functions with formulas, graphs, and mathematical tables / edited by Milton Abramowitz and Irene A. Stegun.*, 10th ed., ser. Applied mathematics series (Washington, D.C.); 55. Washington, D.C.: U.S. Dept. of Commerce : U.S. G.P.O., 1972.

[17] B. R. Mahafza, *Radar Systems Analysis and Design Using MATLAB*, 1st ed. USA: CRC Press, Inc., 2000.

[18] E. F. Knott, *Radar cross section measurements*. Raleigh, NC: SciTech Pub., 2006.

[19] M. A. Richards, J. A. Scheer, and W. A. Holm, *Principles of modern radar*. Raleigh, NC: SciTech Pub., 2010.

[20] D. W. Hess, "Introduction to rcs measurements," in *2008 Loughborough Antennas and Propagation Conference*, 2008, pp. 37–44.

[21] A. V. Oppenheim, R. W. Schafer, and J. R. Buck, *Discrete-Time Signal Processing (2nd Ed.)*. USA: Prentice-Hall, Inc., 1999.

[22] F. J. Harris, "On the use of windows for harmonic analysis with the discrete fourier transform," *Proceedings of the IEEE*, vol. 66, no. 1, pp. 51–83, 1978.

[23] M. A. Richards, *Fundamentals of Radar Signal Processing*. McGraw-Hill Professional, 2005.

[24] R. Harrington, "Origin and development of the method of moments for field computation," *IEEE Antennas and Propagation Magazine*, vol. 32, no. 3, pp. 31–35, 1990.

[25] "User manual/working with CADFEKO," Altair Engineering Inc., May 2014.

[26] B. Kolundzija, M. Tasic, D. Olcan, D. Zoric, and S. Stevanetic, "Full-wave analysis of electrically large structures on desktop pcs," in *CEM'11 Computational Electromagnetics International Workshop*, 2011, pp. 122–127.

[27] A. C. Polycarpou, *Introduction to the Finite Element Method in Electromagnetics*, 1st ed., ser. Synthesis Lectures on Computational Electromagnetics. San Rafael, Calif. (1537 Fourth Street, San Rafael, CA 94901 USA): Morgan & Claypool Publishers, 2006, vol. 4., no. 1.

[28] J. Oden and J. Reddy, *An introduction to the mathematical theory of finite elements.*, ser. Pure and applied mathematics. New York: Wiley, 1976.

[29] "HFSS getting started guides/radar cross section," HFSS, 2015.

[30] *Pyramidal Absorbers- AEP Broadband Series*, Microwave Vision Group, 2019.

[31] *Certificate of Calibration*, Century Metal Spinning Company, Bensenville, IL, USA.

[32] F. de Daran, V. Vigneras-Lefebvre, and J. P. Parneix, "Modeling of electromagnetic waves scattered by a system of spherical particles," *IEEE Transactions on Magnetics*, vol. 31, no. 3, pp. 1598–1601, 1995.

[33] J. Bruning and Yuen Lo, "Multiple scattering of em waves by spheres part i–multipole expansion and ray-optical solutions," *IEEE Transactions on Antennas and Propagation*, vol. 19, no. 3, pp. 378–390, 1971.

[34] S.-Y. Kim and S.-S. Kim, "Design of radar absorbing structures utilizing carbon-based polymer composites," *Polymers & polymer composites*, vol. 26, no. 1, pp. 105–110, 2018.

[35] R. Zoughi and B. Zonnefeld, "Permittivity characteristics of kevlar, carbon composites, e-glass, and rubber (33% carbon) at x-band (8–12 ghz)," 1991.

[36] R. Taipalus, T. Harmia, M. Zhang, and K. Friedrich, "The electrical conductivity of carbon-fibre-reinforced polypropylene/polyaniline complex-blends: experimental characterisation and modelling," *Composites science and technology*, vol. 61, no. 6, pp. 801–814, 2001.

[37] A. Soltane, G. Andrieu, and A. Reineix, "Monostatic radar cross-section estimation of canonical targets in reverberating room using time-gating technique," in *2018 International Symposium on Electromagnetic Compatibility (EMC EUROPE)*, 2018, pp. 355–359.

[38] C. L. Mack and B. Reiffen, "RF characteristics of thin dipoles," *Proceedings of the IEEE*, vol. 52, no. 5, pp. 533–542, 1964.

[39] S. D. Blunt and K. Gerlach, "Adaptive pulse compression via mmse estimation," *IEEE Transactions on Aerospace and Electronic Systems*, vol. 42, no. 2, pp. 572–584, 2006.

[40] Bin Zhao, L. Kong, Mei Yang, and G. Cui, "Adaptive pulse compression for stepped frequency continuous-wave radar," in *Proceedings of 2011 IEEE CIE International Conference on Radar*, vol. 2, 2011, pp. 1780–1783.